

A Spatial Light Modulator for Steering Quantum Walks with Single-Site Precision

Masterarbeit in Physik von

Alexander Knieps

angefertigt im

Institut für Angewandte Physik Bonn

vorgelegt der

Mathematisch-Naturwissenschaftlichen Fakultät

der

Rheinischen Friedrich-Wilhelms-Universität Bonn

am

31.03.2017

1. Gutachter: Prof. Dr. Dieter Meschede
2. Gutachterin: Priv.-Doz. Dr. Elisabeth Soergel

Abstract

This master thesis investigates the potential application of a Liquid Crystal on Silicon Spatial Light Modulator for control of the coin flip operation in a two-dimensional quantum walk. First, the phase noise characteristics of two such modulators from different manufacturers are analyzed. Then an optical setup is constructed to perform holography using phase modulation. The evaluation of this setup verifies pattern generation capability and shows further directions for improvement of image quality.

Contents

0	List of Abbreviations	6
1	Introduction	7
1.1	The Quantum Walk	7
1.2	Quantum Walks with Neutral Atoms: A State Dependent Atomic Lattice . .	7
1.3	Extending the Lattice to Two Dimensions	9
1.4	Modifying the Coin State with Single Site Precision	9
2	Spatial Light Modulators	11
2.1	Digital Micromirror Devices	11
2.2	Liquid Crystal Devices	11
2.2.1	Twisted Nematic Configuration	13
2.2.2	Parallely Aligned Nematic Configuration	13
2.2.3	Structure of a Liquid Crystal on Silicon Modulator	14
2.3	Operation Modes of Liquid Crystal Modulators	14
2.3.1	Phase Modulation	15
2.3.2	Polarization and Amplitude Modulation	15
2.4	Noise Sources in Liquid Crystal Devices and its Suppression	15
3	Phase Noise Characterization of Two LCoS Modulators	17
3.1	Characterization Setup	17
3.2	DC Phase Response	19
3.3	Laser Intensity Noise Subtraction	19
3.4	Phase Noise Analysis	22
4	Inline Holography using Spatial Light Modulators	24
4.1	Fourier Optics	24
4.1.1	Influence of Pixel Structure	25
4.2	The Gerchberg-Saxton Algorithm for Phase Pattern Computation	29
4.3	Minor Modifications of the Algorithm	29
4.4	The Problem of Optical Phase Vortices	32
4.5	Alternative Algorithm Optimized for Optical Tweezers	32
4.5.1	Performance Analysis for 100 Tweezers	33
5	Implementing Inline Holography for the Two-Dimensional Quantum Walk Experiment	33
5.1	The Optical Layout	33
5.1.1	Lens Configurations	38
5.2	Simulated Imaging Performance	39
5.3	Calibration of the Spatial Light Modulator	45
5.3.1	Linear Phase Gain	45
5.3.2	Beam Profile and Objective Aperture	45
5.3.3	Phase Distortions	46

6	Image Analysis of Example Patterns	48
6.1	Point Spread Function	48
6.2	Four Points	49
6.3	Rectangular pattern	50
6.4	Complex Binary Shape	52
6.5	Square in Alternative Imaging Configuration	54
6.6	Complex Binary Shape in Alternative Imaging Configuration	54
7	Summary and Outlook	56
	References	57
	Acknowledgements	60
	Declaration of Authorship	61

0 List of Abbreviations

DMD	Digital Micromirror Device
IFT	Iterative Fourier Transform
IFTA	Iterative Fourier Transform Algorithm
LC	Liquid Crystal
LCoS	Liquid Crystal on Silicon
PAN	Parallely Aligned Nematic
TN	Twisted Nematic

1 Introduction

Modern computation systems have proven themselves to be powerful tools. Large-scale computing systems are used to approach complex systems like global weather prediction [18], the folding of proteins [9] and the human brain [21]. At the same time, machine learning methods are applied day-to-day tasks such as image classification [20] and translation [19] which before could only be performed by humans. However, when approaching the problem of many-particle quantum mechanics, even those powerful systems are stopped by the barrier of exponential complexity growth. It was in the face of this problem that the concept of quantum simulation was proposed [11]. Instead of a numerical evaluation, the quantum system in question is mapped onto a controlled model system. Examples of this include the simulation of frustrated magnetism [17, 30] and the hydrogen molecule [10].

1.1 The Quantum Walk

The quantum walk is a quantum mechanical analogon to the classical random walk. It extends the probabilistic nature of the random walk by quantum effects like interference and state entanglement [15]. Quantum walks are generally distinguished broadly into two categories [32]:

- **Discrete Time Quantum Walks** are built out of a walker (a countable quantum system representing position space) and a coin (a finite quantum system representing internal state). Time evolution is described by a unitary operator applied to walker and coin at each time step.
- **Continuous Time Quantum Walks** use - instead of the coin and the unitary time evolution operator - a Hamiltonian operator directly applied to the walker's state space. The time evolution of a continuous time quantum walk is given by the corresponding Schrödinger equation.

The underlying domain of both kinds of walks is usually discrete due to the close relationship between discrete domains and computation states of classical algorithms [32]. The basic idea of evaluating the final distribution from a given initial state (see for example [5]) can be extended by intermediate measurements using for example negative measurement techniques [24].

1.2 Quantum Walks with Neutral Atoms: A State Dependent Atomic Lattice

Our group uses a quantum walk scheme where neutral Cesium are trapped into a state-dependent optical lattice [26]. The coin state is encoded using the single valence electron's spin. Alternative approaches include trapped ions [33] or the photons guided in coupled waveguides [22].

The three lowest electronic states of an alkali atom are $^2S_{1/2}$ (Spin 1/2, no angular momentum), $^2P_{1/2}$ (Spin 1/2, angular momentum 1, singlet) and $^2P_{3/2}$ (Spin 1/2, angular momentum 1, triplet). The excitation energies from the ground state are much larger than the fine structure splitting between the two excited states [29]. Illuminating an atom with a light field frequency-detuned to the atomic state (with a detuning so large that excitation probabilities can be neglected) then shifts the atomic levels by [23, p. 5]:

$$\Delta E = \frac{6\pi c^2 \Gamma}{\omega_0^3 \Delta} I \quad (1)$$

where $\Delta = \omega - \omega_0$ is the detuning of the laser with respect to the atomic transition, I is the light intensity (power/area) and Γ is the natural line width of the respective transition.

Consider the following setting: The ground state of the atom is illuminated with σ_+ light red detuned to the $^2S_{1/2} \rightarrow ^2P_{3/2}$ (D_2 line) transition and blue detuned to the $^2S_{1/2} \rightarrow ^2P_{1/2}$ (D_1 line) transition.

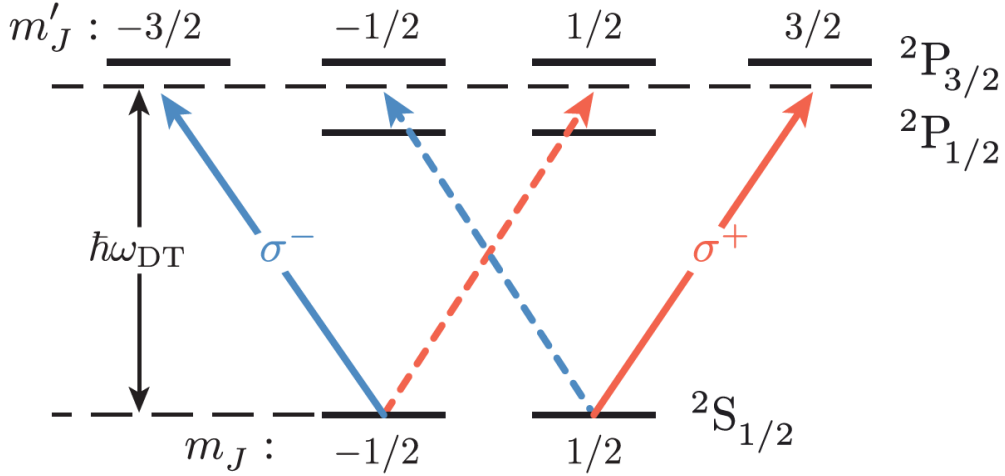


Figure 1: State dependent optical lattice scheme, taken from [23, p. 18]

The $m_S = m_J = -\frac{1}{2}$ state can undergo both transitions, so it is subjected to two opposing light shifts. However, the $m_S = +\frac{1}{2}$ state is only subject to the red detuned D_2 illumination (because an $m_{J'} = \frac{3}{2}$ sub-state of the $^2P_{1/2}$ state does not exist). By choosing the wavelength of the illuminating light so that the light shifts on the $m_S = -\frac{1}{2}$ state cancel, one has created an optical lattice attracting only one of the spin states. A second optical system coupling only to the other spin-state can then be constructed from σ_- light at the same wavelength. This wavelength where the opposing light shifts cancel shall from now on be dubbed as the *magic wavelength*. For an illustration of this principle see figure 1.

The treatment of the atomic states in terms of purely electronic fine-structure states neglects the interaction between the electron and the atom's nucleus. To incorporate these effects one needs to look into the atomic hyperfine states. Suitable candidates for Cesium are

$$\begin{aligned} |F = 4, m_F = 4\rangle &= \left| I = \frac{7}{2}, m_I = \frac{7}{2} \right\rangle \otimes \left| S = \frac{1}{2}, m_S = \frac{1}{2} \right\rangle \\ |F = 3, m_F = 3\rangle &= \sqrt{\frac{7}{8}} \left| I = \frac{7}{2}, m_I = \frac{7}{2} \right\rangle \otimes \left| S = \frac{1}{2}, m_S = -\frac{1}{2} \right\rangle \\ &\quad + \sqrt{\frac{1}{8}} \left| I = \frac{7}{2}, m_I = \frac{5}{2} \right\rangle \otimes \left| S = \frac{1}{2}, m_S = \frac{1}{2} \right\rangle \end{aligned}$$

For these states one can find a magic wavelength where $|F = 4, m_F = 4\rangle$ couples only to the σ_+ component while $|F = 3, m_F = 3\rangle$ still couples predominantly to the σ_- component. A one-dimensional optical lattice can then be constructed from counter propagating light beams at the magic wavelength. Modulating the phases of the left- and right-handed component of one of the beams then allows to shift the two lattices independently [23].

1.3 Extending the Lattice to Two Dimensions

In the previous section we saw how to construct a one-dimensional quantum walk system using a state dependent atomic lattice. One can extend this concept to two-dimensional lattices. This can be achieved using two counter-propagating beams (which can have the phases of their left- and right-handed polarizations modulated) as well as a third orthogonal beam (with fixed phases). The functionality of this scheme can be already seen using a simplified scalar treatment (for one of the polarizations). For a rigorous treatment please refer to [6].

The complex field amplitude for either left- or right-handed polarization (assuming equal beam amplitudes) can be written as

$$\begin{aligned} E &\propto e^{2\pi i k x + i \Delta \varphi_1} + e^{-2\pi i k x + i \Delta \varphi_2} + e^{2\pi i k y} \\ &= 2 \cos(2\pi k x + \Delta \varphi_1 - \Delta \varphi_2) \cdot e^{i(\Delta \varphi_1 + \Delta \varphi_2)} + e^{2\pi i k y} \\ |E|^2 &\propto (2 \cos(2\pi k x + \Delta \varphi_1 - \Delta \varphi_2) + \cos(2\pi k y - (\Delta \varphi_1 + \Delta \varphi_2)))^2 + (\sin(2\pi k y - (\Delta \varphi_1 + \Delta \varphi_2)))^2 \\ &\propto \\ &= (2 \cos(2\pi k x + \Delta \varphi_1 - \Delta \varphi_2))^2 + 4 \cos(2\pi k x + \Delta \varphi_1 - \Delta \varphi_2) \cos(2\pi k y - (\Delta \varphi_1 + \Delta \varphi_2)) + 1 \end{aligned}$$

where $k = \frac{1}{\lambda}$ is the inverse wavelength and $\Delta \varphi_{1,2}$ are the phase delays applied to the two counter-propagating beams. This is maximized when

- $\cos(2\pi k x + \Delta \varphi_1 - \Delta \varphi_2) = 1 \wedge \cos(2\pi k y - (\Delta \varphi_1 + \Delta \varphi_2)) = 1$ or
- $\cos(2\pi k x + \Delta \varphi_1 - \Delta \varphi_2) = -1 \wedge \cos(2\pi k y - (\Delta \varphi_1 + \Delta \varphi_2)) = -1$

which is fulfilled when

$$\begin{aligned} (x, y) &= \frac{\lambda}{2} (n_1, n_2) + \frac{\lambda}{2\pi} (\Delta \varphi_2 - \Delta \varphi_1, \Delta \varphi_1 + \Delta \varphi_2) \\ &n_1 + n_2 \text{ even} \end{aligned}$$

This implies a diagonal lattice of lattice constant

$$d = \frac{\lambda}{\sqrt{2}}$$

that can be shifted by modulating the phases $\Delta \varphi_{1,2}$ of the counter-propagating beams.

1.4 Modifying the Coin State with Single Site Precision

The levels ($|F = 3, m_F = 3\rangle$ and $|F = 4, m_F = 4\rangle$) of the two-level-system are only separated by a hyperfine structure splitting of $9.19 \text{ GHz} \cdot \hbar$ [29]. Driving this transition directly requires

microwave radiation of a wavelength of $\lambda \approx 3.3$ cm. At this wavelength the distance between two adjacent lattice sites can no longer be resolved. In order to still be able to address single lattice sites one must find a way to include optical wavelengths into the driving scheme. This can be achieved by shifting the energy levels using an optical transition. The required power to perform such an addressing scheme on the Cesium D_1 line can be calculated from the duration of the microwave pulse. A Gaussian pulse of duration τ has a line-width of $\frac{1}{2\tau}$. Using equation 1 ($\Delta E = \frac{6\pi c^2}{\omega_0^3} \frac{\Gamma}{\Delta} I$) one can determine the required intensity

$$I = \frac{\hbar\omega_0^3\Delta}{6c^2\tau\Gamma}$$

Assuming that an area of n by n lattice sites is to be illuminated, the total power required is given by:

$$\begin{aligned} P &= n^2 d^2 I \\ &= n^2 d^2 \frac{\hbar\omega_0^3\Delta}{6c^2\tau\Gamma} \end{aligned}$$

The lattice constant of the 2D optical lattice is $d = \frac{866 \text{ nm}}{\sqrt{2}} = 612$ nm (see [6]). A reasonable assumption for the illuminated area is a 50x50 lattice site grid. Due to technical reasons, the most likely optical transition to be used for inducing the light shifts is the D_1 ($6^2S_{1/2} \rightarrow 6^2P_{1/2}$) transition. This transition has a natural line-width of $\Gamma_{D_1} = 2\pi \cdot 4.56$ MHz and a circular frequency of $\omega_0 = 2\pi \cdot 335$ THz. For a pulse duration of 5 μ s and a detuning of 10 line-widths one obtains a required laser power of $P = 3.4$ nW.

An alternative approach would be to use a two-photon transition via a virtual state near the $6^2P_{1/2}$ -state. As shown in [2], this can be achieved using two lasers. In order to resonantly drive the hyperfine transition, the frequency difference between the two lasers has to match the hyperfine splitting. If the lasers are detuned sufficiently from the D_1 transition, the excitation into the $^2P_{1/2}$ state is suppressed without suppressing the hyperfine transition itself.

Both of these schemes cover the light-atom interaction component of addressing. Nonetheless, the question remains how the optical patterns for the addressing mechanism should be created. To achieve single-site resolution, an objective with a high numerical aperture of 0.92 is used [25]. The atoms are cooled using an optical molasse [3] on the D_2 line. The scattered photons are used for fluorescence imaging. The addressing system can simultaneously operate on the D_1 line using the same objective. The imaging (852 nm [29]) and addressing light (896 nm [29]) are separated using a dichroic mirror.

2 Spatial Light Modulators

The term spatial light modulator applies to a variety of different devices, all of which share a single property - they allow to address a subsection of an incident light beam and modify its properties. Depending on type and configuration of the device in question, polarization, amplitude and phase of the incident light field can be modulated. These spatially varied modifications allow to create a variety of useful effects, including aberration correction [7], three-dimensional point-spread functions [4], beam steering [8] and hologram generation [35]. The devices used in these applications can be distinguished into two different categories.

2.1 Digital Micromirror Devices

A Digital Micromirror Device - abbreviated as DMD - is an array of mirrors each mounted on a tiny hinge. Each mirror can be individually tilted (e.g. by varied electrostatic forces) permitting control over the direction that each mirror pixel reflects the light into. The mirror states can be used to create - up to the resolution of the device - arbitrary diffraction gratings. Because the mirrors are - in their rest positions - angled towards the pixel matrix, they reflect not into the 0th order of the diffraction grating formed out of the mirror array. The phase shift between each mirror's reflection combined with the wide point spread function of an individual mirror allows to create holograms by switching pixels interfering constructively in the desired directions to the "on"-state, while tilting others to the "off"-state. An illustration of the underlying machinery can be seen in figure 2.

2.2 Liquid Crystal Devices

An alternative technology is based on liquid crystals. Liquid crystals are substances which are macroscopically in a liquid phase (vanishing shear modulus) but still exhibit microscopic order at room temperature. A nematic liquid crystal is a phase where this long range correlation is limited to orientation, while the positional distribution resembles that of a liquid. Nematic phases (due to their low viscosity allowing quick state switching) make up the biggest share of liquid crystal display technology [34].

The liquid crystal molecules are usually oriented using Van-der-Waals interactions between the liquid crystal molecules and the domain walls. By modifying the shape of the border surfaces of a liquid crystal segment, one can anchor the molecules into specific directions. This is commonly done by rubbing the alignment surface in the target direction [34]. The strong anisotropy of the liquid crystal molecules' polarizability however has two additional useful effects: On the one hand this phenomenon results in a strong birefringence of the liquid crystal. This implies that by achieving control over the molecular orientation one can modify polarization or phase of light passing through the liquid crystal cell. On the other hand this anisotropy leads to liquid crystal molecules orienting themselves along external electric fields. Since this force competes with the Van-Der-Waals interactions between the molecules and the anchoring surfaces, modulating the field strength grants control of the equilibrium orientation. Combining these three properties give the basic receipt for liquid crystal based light modulation:

- Specify the natural rest orientation of the molecules using the anchoring surfaces
- Modify the orientation using an external electric field
- Use the orientation of the liquid molecule to modify light properties

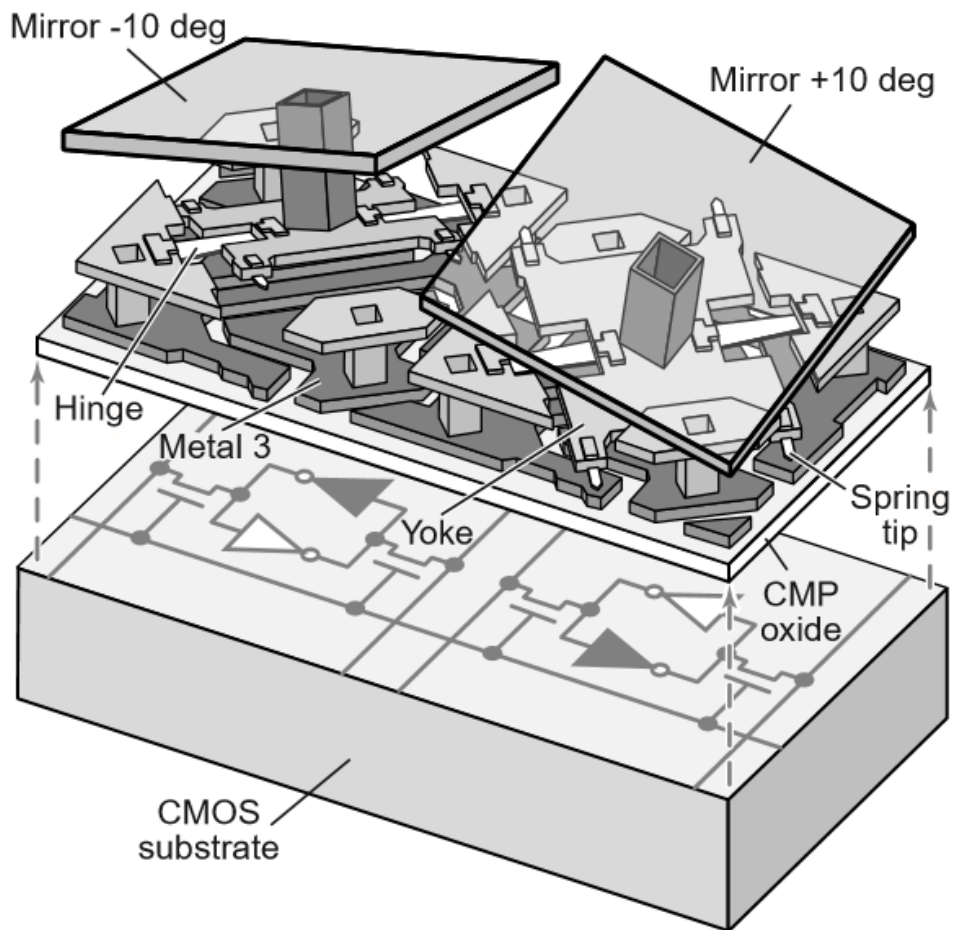


Figure 2: Two DMD pixels (mirrors shown as transparent) [13]

Two variants of this technology are outlined below. Both rely on the nematic phase of the liquid crystal materials.

2.2.1 Twisted Nematic Configuration

The twisted nematic configuration is frequently used in the construction of liquid crystal displays [34]. The anchoring surfaces on both ends of the liquid crystal region are oriented at an angle of 90° towards each other. Without external disturbance, the molecular orientation forms a 90° quarter-helix over the length of the display. Mostly independently of wavelength, the polarization of incoming light will follow this 90° tilt. When an electric field is turned on – which is usually oriented in parallel to the first anchor surface’s orientation – the molecules orient along the light propagation direction and all birefringence effects break down. An illustration of this effect can be seen in figure 3. The black arrows refer to the alignment directions for the anchoring forces. Adding crossed polarizers converts the polarization modulator into an amplitude modulation. This technique has limited applications in phase-modulation due to polarization crossover [34].

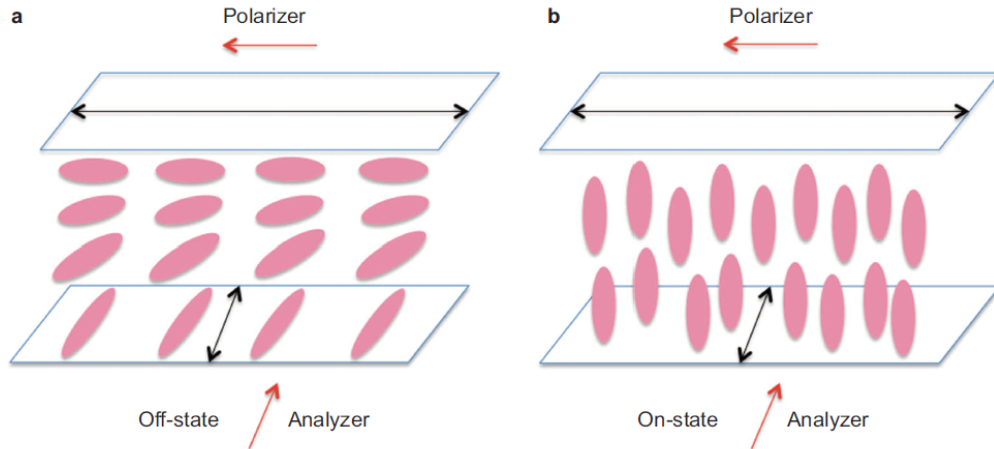


Figure 3: Schematic of a liquid crystal cell in Twisted Nematic configuration, with the electric field switched off (a - left) and switched on (b - right) [34]

2.2.2 Parallely Aligned Nematic Configuration

The Parallely Aligned Nematic (PAN) mode, sometimes referred to as Electrically Controlled Birefringence (ECB) opts instead to orient the molecules along a common axis [34]. The natural (off-state) molecular orientation is chosen to be parallel to the alignment surfaces. This makes the liquid crystal simply appear as a birefringent material. The on-state electric field is oriented perpendicular to the anchor surface. Thus the electric field reduced the effective birefringence of the crystal seen by the light propagating to the cell (if the light is perpendicular to the anchoring surfaces).

The biggest advantage of this configuration is that it has great operational flexibility. Depending on application, it can be used to modulate amplitude, polarization or phase of the incident light (see section 2.3).

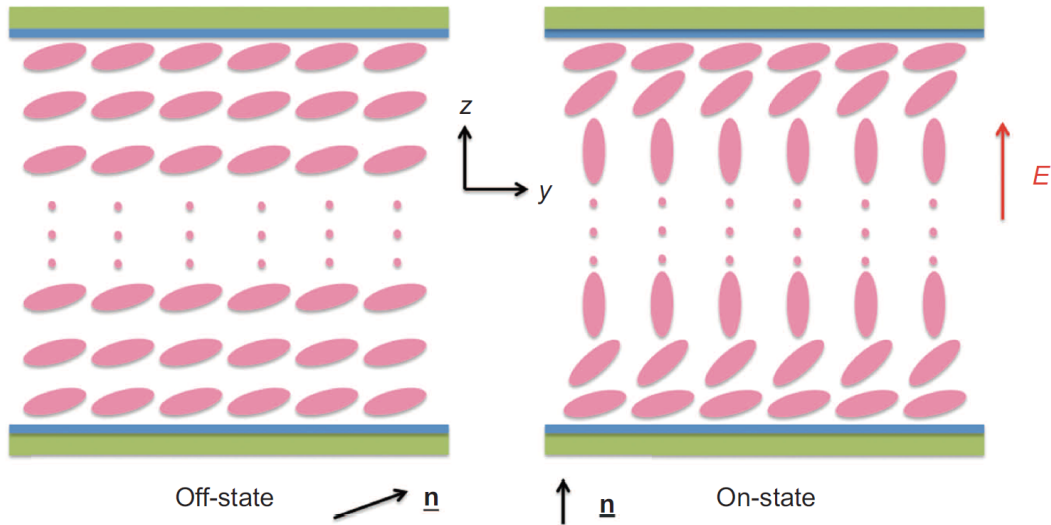


Figure 4: PAN / ECB mode of a liquid crystal display [34]

2.2.3 Structure of a Liquid Crystal on Silicon Modulator

Instead of using two transparent end electrodes for the spatial light modulator, one can also use a reflective back-electrode. The electronics to drive and control the electric field can then be placed behind the light modulating system, which permits increased pixel densities and higher drive currents. This idea gives rise to the Liquid Crystal on Silicon (LCoS) architecture, where the front plane is usually a shared grounded and transparent electrode and the back-electrode drives the electric field in PAN configuration (see section 2.2.2). See figure 5 for a cross section of such a design.

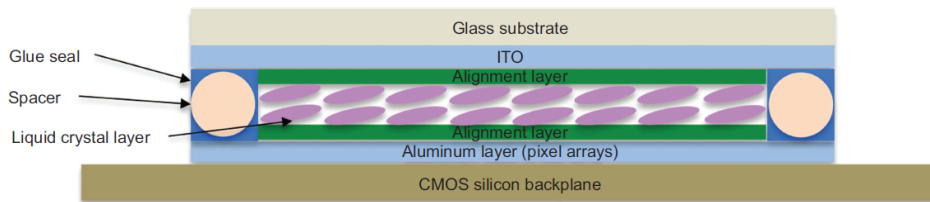


Figure 5: Schematic of a Liquid Crystal on Silicon Spatial Light Modulator [34]

2.3 Operation Modes of Liquid Crystal Modulators

For all further discussions I will limit the scope to PAN (2.2.2) LCoS (2.2.3) SLMs. As hinted at in section 2.2.2, one of the hallmarks of this configuration is its operational flexibility. In the following the different operational modes are discussed in detail.

2.3.1 Phase Modulation

The PAN operational mode (2.2.2) operates by modulating the effective birefringence of the LC seen by light passing through. More specifically, it modulates the birefringence by tilting the extraordinary axis of refraction towards the light's k-vector. If the incident light is linearly polarized and its polarization axis corresponds with the extraordinary axis of the LC molecules (in the off-state), then the light field is not influenced by the birefringence. However, it sees an electric field dependent index of refraction. This means that the propagation of the light can be variably delayed, by modifying its coupling to the LC molecules (and their dipole moments). The off-state corresponds to maximum delay. Note that the phase change $\Delta\varphi$ is wavelength dependent and related to the wavelength-independent propagation ΔT delay by:

$$\begin{aligned}\Delta\varphi &= 2\pi\nu\Delta T \\ &= 2\pi\frac{c}{\lambda}\Delta T \\ &\Leftrightarrow \\ \lambda\Delta\varphi &= 2\pi c\Delta T\end{aligned}\tag{2}$$

2.3.2 Polarization and Amplitude Modulation

When light passes through a birefringent material one of its polarization components acquires an extra phase $\Delta\varphi$ as in equation (2). This leads to a change in polarization state. For a linear 45° input polarization $\alpha = \beta = \frac{1}{\sqrt{2}}$ the transformation results in

$$\begin{aligned}&\frac{1}{\sqrt{2}}(|\uparrow\rangle + |\leftrightarrow\rangle) \\ \rightarrow &\frac{1}{\sqrt{2}}(|\uparrow\rangle + e^{i\Delta\varphi}|\leftrightarrow\rangle)\end{aligned}$$

At $\Delta\varphi = \pi$ this is the opposite linear 45° polarization state, while the delays $\Delta\varphi = \pm\frac{\pi}{2}$ correspond to circular polarization states. When inserting a polarization plate aligned to the $(|\uparrow\rangle + |\leftrightarrow\rangle)$ polarization behind the modulator, the passing light retains the intensity of

$$\begin{aligned}I &\propto \frac{1}{4} |(|\uparrow\rangle + |\leftrightarrow\rangle) \cdot (|\uparrow\rangle + e^{i\Delta\varphi}|\leftrightarrow\rangle)|^2 \\ &= \frac{1}{4} |1 + e^{i\Delta\varphi}|^2 \\ &= \frac{1}{4} \left((1 + \cos(\Delta\varphi))^2 + \sin^2(\Delta\varphi) \right) \\ &= \frac{1}{4} (2 + 2\cos(\Delta\varphi)) \\ &= \frac{1 + \cos(\Delta\varphi)}{2}\end{aligned}$$

This transforms the polarization modulation into a sine-shaped amplitude modulation.

2.4 Noise Sources in Liquid Crystal Devices and its Suppression

Liquid crystals are no perfect isolators. When subject to a static electric field, the molecules are subject to electrolysis, which in time destroys the cell. To prevent this, the electric field

is frequently flipped. The molecules couple to the field via an induced dipole. That coupling depends only on the squared magnitude of the field, not on its sign. Since the electrons have orders of magnitude higher mobility than the molecule itself, the sign flip has negligible effects on the LC molecules. However, instantaneously flipping the field to opposite direction, but equal magnitude, is a technically challenging goal. In practice two concessions have to be made

- At opposite sign the field magnitude can differ slightly (due to technical imperfections in the driver)
- The transition is not instantaneous, thus during the transition time the molecules see a reduced electric field

These two effects lead to a phase modulation flicker at the switching frequency (and its harmonics) superimposed on the desired phase modulation. There are two principal methods to suppress this effect:

- Reduce electric field noise. Improving the first problem requires more sophisticated electronics, while the second cause requires higher drive currents (without overdriving the system). Since these goals are beyond some point at odds with each other this is a difficult approach.
- Suppress the flicker using the molecule's inherent inertia: Since the molecules are driven by the induced dipole in second order in time, their inertia imposes a low pass filter on the phase flicker. This low pass effect is related to the system's response time. Increasing the flicker base frequency and lengthening the system's intrinsic response time both serve in reducing the flicker amplitude. The response time limit itself can then be overcome by applying a controlled overdrive to the device (Boulder Nonlinear Systems specializes into fast SLMs using this technology [31]).

3 Phase Noise Characterization of Two LCoS Modulators

When using the spatial light modulator to project a light pattern onto quantum walkers, the phase noise inherent in these devices has two detrimental effects. On the one hand side the intensity fluctuations can lead to heating of the atoms in the lattice. If the noise has an intensity peak at one of the motional trap frequencies (or its harmonics), then this noise component is resonantly absorbed and the heating effect is magnified. On the other hand side intensity fluctuations in the target pattern (which, if using the imaging scheme described in section 4, can be caused by phase fluctuation) lead to relative dephasing of the different lattice sites. This will, over time, cause decoherence of the quantum walk. For this reason it was instrumental to evaluate the phase fluctuation of candidate devices before purchase.

Two companies had the generosity to provide sample devices for testing:

- Hamamatsu provided an instance of their X-13268, an OEM variant of their X-13267 series intended for usage as a module in more complex devices. This variant series lacked a protective casing for the circuit board and had a slightly modified control setup, but was otherwise functionally identical to the laboratory version. Hamamatsu offers a wide array of LCoS based spatial light modulators, but their high-resolution device has lower phase stability compared to the tested device. However they offer a wide variety of customizations, including a series of dielectric mirrors replacing the standard aluminum back-plane.
- Santec provided an older generation device of their SLM-100 series for testing. This device combines a high resolution (1440x1050) with a high phase stability and competitive pricing.

3.1 Characterization Setup

I tested the modulators using the amplitude modulation scheme presented in section 2.3.2. The laser light source was an 850nm diode laser operated in Littrow configuration (Axcel Photonics M9-852-0150-S3P). The light of this laser was coupled through an optical isolator. Using a pair of $\lambda/4$ -plates (due to quarter-wave plates being more available than half-wave plates at the time) and a polarizing beam-splitter I then split the laser beam into a probe and a reference beam. The reference beam was focused onto a ThorLabs PDA 10A-ECr photodiode. The probe beam's polarization was then adjusted using another pair of quarter-wave plates and a polarization plate. With a telescope formed out of a lens immediately behind the optical isolator and a 1m planar-convex lens the probe beam was widened to an estimated waist of ≈ 1 cm in order to cover the active area of both modulators. It was then directed onto the modulator at minimal possible reflection angle, and the reflected light was guided through an analyzer plate and focused onto a ThorLabs PDA 10A-EC photodiode.

A sketch of this setup can be seen in figure 6. The intensity response at the analyzer photodiode has a sinusoidal dependence on the phase modulation. Therefore around the extrema the setup is insensitive to phase noise. To compensate this both behind the polarizer as well as in front of the analyzer quarter-wave plates can be introduced to switch between 45° linear and circular polarization. Each quarter-wave plate shifts the insensitive region by $\frac{\pi}{2}$, which allows the system to be fully sensitive by aggregating measurements from multiple configurations.

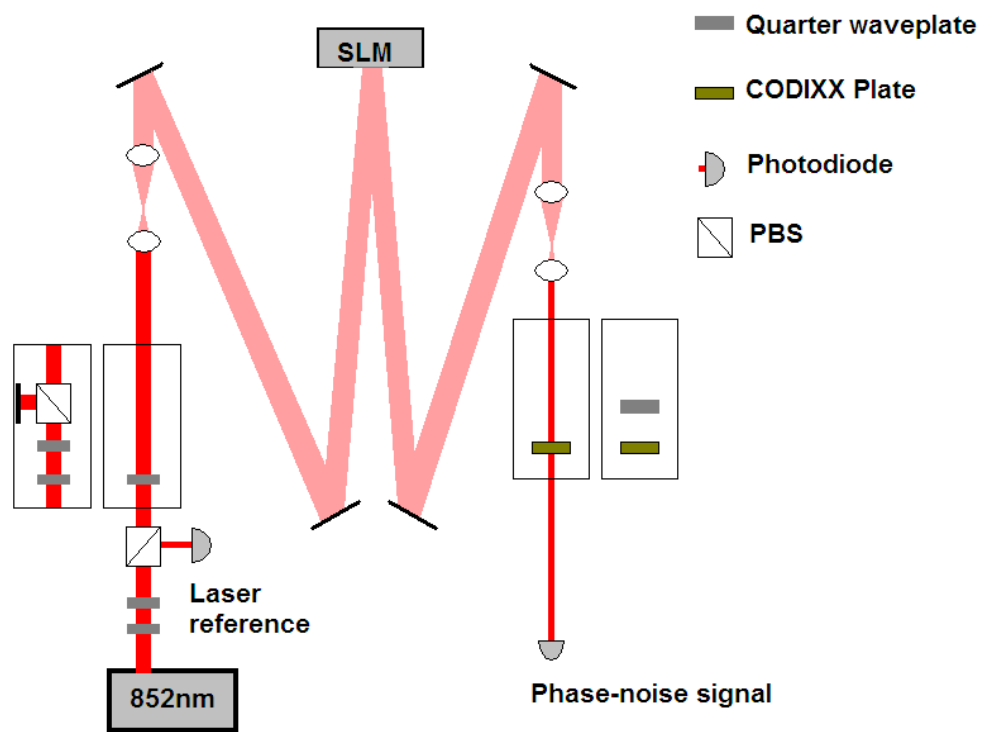


Figure 6: Phase noise analysis testbed

3.2 DC Phase Response

Both spatial light modulators are addressed as a computer screen, which is connected to the controlling PC via a DVI-D cable. In this setup, a variable uniform phase modulation was applied to all pixels. The correspondence between the 8-(Hamamatsu) respectively 10-bit (Santec) number sent to a pixel and the phase modulation at a given wavelength is unknown and needs to be measured. Additionally, the response behavior of the photodiode is unknown and needs to be calibrated. Both of these measurements are performed by setting all pixels of the modulator to the same phase modulation value, and then iterating through all possible values and measuring the intensity response (0-255 for the Hamamatsu device, 0-1023 for the Santec modulator) on the analyzer photodiode. The response curves are outlined in figure 7. Error bars on input data are not shown as both statistical fluctuations as well as imprecisions of the oscilloscope were in the millivolt regime. The x-axis represents the integer-number sent to the modulator device to request a given phase modulation. This number will in the following be referred to as j .

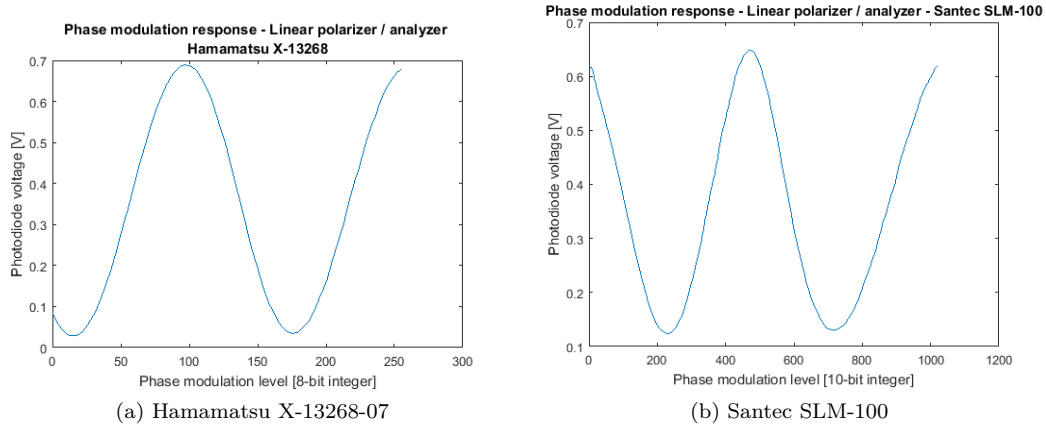


Figure 7: Response of the analyzer photodiode over phase modulation levels - All polarizations linear

These curves were then fit with the function model $V(j) = V_0 + \cos(\alpha \cdot j + \beta)$ to obtain analytic expressions of the response curve. The analysis setup for the Hamamatsu device showed no visible deviations between the fit and the data, while significant deviations were visible on the measurements curves for Santec’s device. This might be due to Santec’s modulator being an older overused demo device, while the modulator from Hamamatsu was less frequently used (due to being an OEM demo device). Because of the strong deviations, I decided not to use the fit function to calibrate the setup, and instead to use the data directly for calibrating the phase noise sensitivity.

3.3 Laser Intensity Noise Subtraction

Since the setup was built from the beginning to provide a laser intensity reference along with the analyzer data, was to devise a method to compensate intensity fluctuations in the laser beam. In an ideal case the voltage on the analyzer photodiode depends only on the

phase fluctuation:

$$V(t) = \epsilon \cdot I_{\text{laser}} \cdot \cos(\varphi(t))$$

However, as seen before, the transfer function is not exactly a cosine and therefore needs to be represented by a general function (which was measured in section 3.2):

$$V(t) = \epsilon \cdot I_{\text{laser}} \cdot f(\varphi(t))$$

As seen in section ??, the trace does not meet the expectations of such an assumption. In addition, one can consider the laser's output intensity noise as a noise component:

$$V(t) = \epsilon \cdot I_{\text{laser}}(t) \cdot f(\varphi(t))$$

Assuming the intensity fluctuations are small, the total fluctuation can be linearized:

$$\begin{aligned} V(t) &\approx \langle V \rangle \\ &+ \epsilon \cdot \langle I_{\text{laser}} \rangle \cdot f'(\langle \varphi \rangle) \cdot (\varphi(t) - \langle \varphi \rangle) \\ &+ \epsilon \cdot f(\langle \varphi \rangle) \cdot (I_{\text{laser}}(t) - \langle I_{\text{laser}} \rangle) \end{aligned}$$

The first component is the average voltage, the second component is the voltage noise derived from the phase noise, while the third component is the laser noise imprinted on the measurement data. Let's now assume the output voltage of the reference beam photodiode is linearly related to the laser intensity:

$$V_{\text{ref}} = a + b \cdot I_{\text{laser}}$$

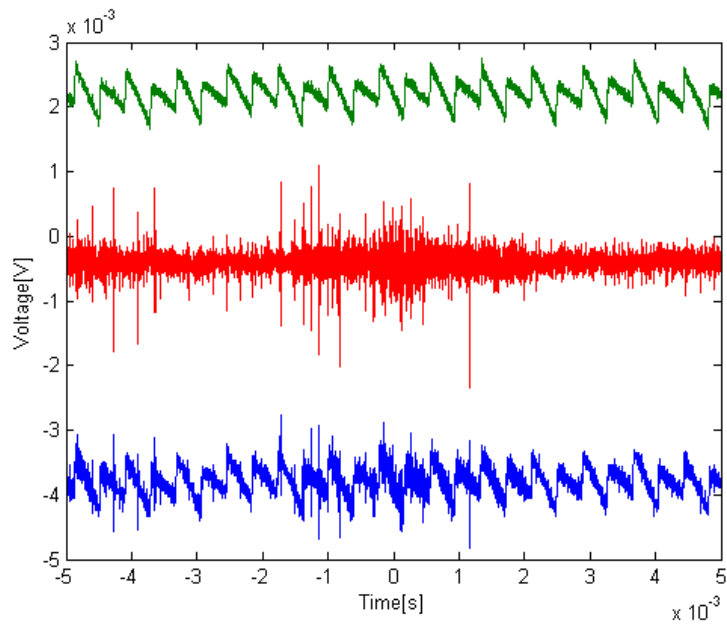
Assuming that the noise on phase and laser intensity are statistically independent (they might be correlated by the power grid) one can project the analyzer noise onto the reference diode noise:

$$\begin{aligned} c_{\text{ref}} &= \frac{\langle V(t) - \langle V \rangle | V_{\text{ref}}(t) - \langle V_{\text{ref}} \rangle \rangle}{\langle V_{\text{ref}}(t) - \langle V_{\text{ref}} \rangle | V_{\text{ref}}(t) - \langle V_{\text{ref}} \rangle \rangle} \\ &\approx \frac{\epsilon}{b} \cdot f'(\langle \varphi \rangle) \end{aligned} \quad (3)$$

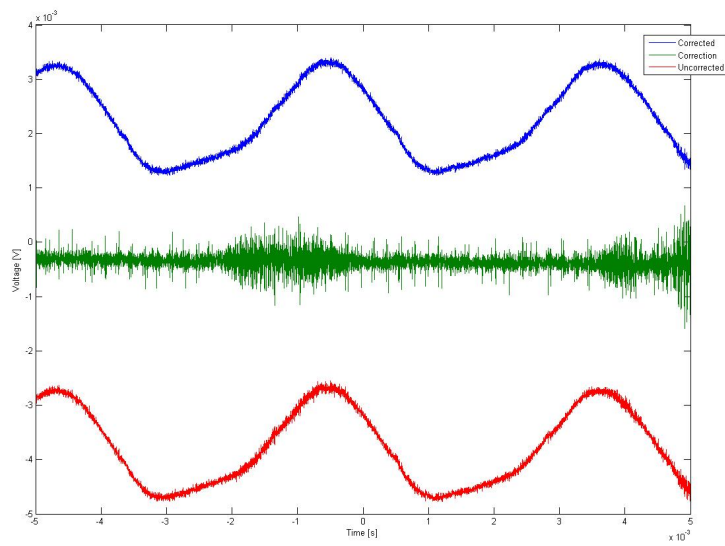
This operation can be best understood when viewing both time series as vectors. For a sufficiently long time series, the randomly parallel components vanish with respect to the ones induced by statistical correlation. The co-moving noise is then the geometrical projection of the dependent on the noise generating time series. Using this idea, the projection coefficient calculated from equation 3 can be used to subtract the induced noise:

$$\begin{aligned} V(t) - c_{\text{ref}}(V_{\text{ref}}(t) - \langle V_{\text{ref}} \rangle) &\approx \langle V \rangle + \epsilon \cdot \langle I_{\text{laser}} \rangle \cdot f'(\langle \varphi \rangle) \cdot (\varphi(t) - \langle \varphi \rangle) \\ &\approx \epsilon \cdot \langle I_{\text{laser}} \rangle \cdot f(\varphi(t)) \end{aligned} \quad (4)$$

Equations 3 and 4 can now be applied to each measurement run to remove (up to first order) the laser intensity noise out of the time traces. In fact (because projection is The results of this process are exemplarily shown in figure 8.



(a) Santec SLM-100



(b) Hamamatsu X-13268

Figure 8: Time trace including laser noise (bottom), laser intensity reference (middle) and corrected signal (top)

3.4 Phase Noise Analysis

In order to calculate the phase noise for each phase modulation level, analyzer photodiode voltage traces were taken on varying time scales. Given the average voltage response $V(j) = \overline{V(j, t)}$ (where j is the integer phase index sent to the modulator, not the direct phase) as well as a linear approximation for the phase level $\varphi = \alpha \cdot j + \beta$ one can relate the standard deviations for the voltage and phase as:

$$\begin{aligned} \sigma_V(j) &= \left| \left[\frac{d}{d\varphi} V(j(\varphi)) \right] (\varphi(j)) \right| \sigma_\varphi(j) \\ &= \left| \frac{dV}{dj}(j) \right| \left| \frac{d\varphi}{dj}(j) \right|^{-1} \sigma_\varphi(j) \end{aligned} \quad (5)$$

$$= \left| \frac{dV}{dj}(j) \right| \alpha^{-1} \sigma_\varphi(j) \quad (6)$$

\Rightarrow

$$\sigma_\varphi(j) = \frac{|\alpha|}{\left| \frac{dV}{dj}(j) \right|} \sigma_V \quad (7)$$

In these equations, $\sigma_V(j)$ represents the standard deviation of the voltage time trace at a given voltage level and σ_φ represents the standard deviation of the optical phase noise. When the voltage response approaches its extrema, the standard deviation computed in 7 diverges. Background noise is magnified in these areas, overshadowing the modulator's fluctuations. To alleviate this, multiple measurements were combined. In between these measurements, quarter-wave plates were introduced to shift the sensitivity curves. The combined set of measurements is (in the ideal case) uniformly sensitive. The measurements are then combined quadratically using the phase noise sensitivities as weights:

$$\begin{aligned} \sigma_{V,k}(j) &= \left| \frac{d}{d\varphi} V_k(j(\varphi)) \right| \sigma_\varphi \\ \sum_{k=1}^n \sigma_{V,k}^2(j) &= \sigma_\varphi^2(j) \cdot \sum_{k=1}^n \left| \frac{d}{d\varphi} V_k(j(\varphi)) \right|^2 \\ &= \alpha^2 \sigma_\varphi^2(j) \sum_{k=1}^n \left| \frac{dV_k}{dj}(j) \right|^2 \\ &\Rightarrow \\ \sigma_\varphi &= |\alpha| \sqrt{\frac{\sum_{k=1}^n \sigma_{V,k}^2}{\sum_{k=1}^n \left| \frac{dV_k}{dj}(j) \right|^2}} \end{aligned}$$

Here j is once again the phase modulation sent to the modulator, $V_k(j) = \overline{V_k(j, t)}$ is the average photodiode voltage measured with respect to this value. $\sigma_\varphi(j)$ is the standard deviation phase noise of the modulator at requested phase modulation $\varphi(j)$ and $\sigma_{V,k}(j)$ is the standard deviation of the time trace for $V_k(j, t)$. Since the analytical fit of the average voltage response $\langle V_k(j, t) \rangle_t$ performed poorly (3.2) the derivative was instead approximated as $\frac{dV}{dj}(j) \approx V(j+1) - V(j)$ and smoothed using a 2nd order Savitzky-Golay-Filter ([27]) with 51 support points (to average out statistical noise).

The results of the phase noise calculation (for time traces of length 10ms) can be seen in figure 9. The modulator vendor is free to choose whether a pixel integer value of 0 represents highest or lowest electric field magnitude. Since no phase noise would be expected in the “off”-state, the phase noise should be expected to be reduced around lower field magnitude values. Both devices show phase stability of 3 mrad in their most stable 2π -regions, and an overall stability of 5 mrad or better. Of special note should be the small kink visible in the 1.5π -region of the Hamamatsu curve. By analyzing the resulting phase noise curves for multiple different oscilloscope time-ranges, I could see that this kink grows significantly for very short timescales. It turns out that this feature is an artifact of the not completely uniform phase noise sensitivity. There is some residual background noise which gets amplified or weakened with the inverse sensitivity (see above calculation).

Based on these results we concluded that both devices offered sufficient phase stability for our experiments. Based on pricing and resolution (concerning phase stability the 800x600 modulator from Hamamatsu was clearly superior to their other options) we decided to buy a SLM-100 from Santec.

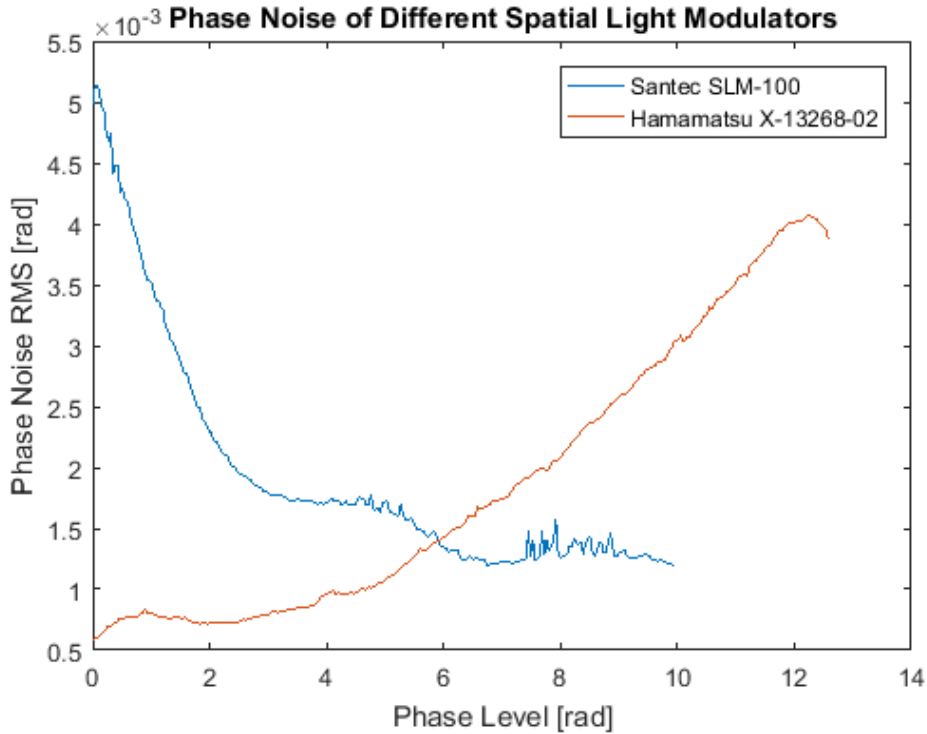


Figure 9: Phase modulation noise in dependence of mean phase modulation level for both tested

4 Inline Holography using Spatial Light Modulators

Many applications of light require some form of beam-shaping or -steering. These include for example video projection, laser-based 3D printing, pattern imprinting, dynamic atom traps and IC wafer production. The simplest method is usually to image a mask or a picture onto a target plane. Such a picture can be created beforehand or dynamically in real-time.

This methods however suffers from power efficiency issues. All the light in a mask pixel not intended to be projected must be thrown away - either absorbed or scattered. If locally bright spots in a mostly dim environment are needed - like it is the case in optical beam steering or single atom addressing - a large percentage (estimated 90% or more) of the power needs to be discarded. This means that for those applications such a simple projector performs significantly worse than a mirror steered by a pair of piezo drivers. And exactly this concept is the basic inspiration for holographic beam-steering.

4.1 Fourier Optics

A steered mirror does not directly act on the intended light distribution. Instead, it acts on a collimated beam, while the modulated plane is the back-focal plane of an objective focusing this beam. The back-focal plane field distribution of an ideal lens can be calculated as

$$\begin{aligned}
 E_{\text{dst}}(x, y) &= \int_{\mathbb{R}^2} E_{\text{lens}}(x', y') \cdot A_{\text{lens}}(x', y') \cdot \exp\left(\frac{2\pi i}{\lambda} \sqrt{f^2 + (x - x')^2 + (y - y')^2}\right) \\
 &\quad \cdot \exp\left(-\frac{2\pi i}{\lambda} \cdot \frac{x'^2 + y'^2}{2f}\right) dx' dy' \\
 &= \int_{\mathbb{R}^2} E_{\text{lens}}(x', y') \cdot A_{\text{lens}}(x', y') \\
 &\quad \cdot \exp\left(\frac{2\pi i}{\lambda} \left[\sqrt{f^2 + (x - x')^2 + (y - y')^2} - \frac{x'^2 + y'^2}{2f}\right]\right) dx' dy'
 \end{aligned} \tag{8}$$

Here E_{lens} is the electric field on the lens while A_{lens} is the aperture cutoff function. x and y represent the position in the far-field plane while x' and y' represent the position on the lens. The first exponential term in equation 8 represents the phase acquired by the free space path between position (x', y') on the lens and (x, y) in the back focal plane. The second exponential term describes the phase picked up from the lens itself.

Approximating the square root term to second order yields an expansion up to an error of $\mathcal{O}\left(\frac{(x-x')^4}{f^3} + \frac{(y-y')^4}{f^3}\right)$:

$$\begin{aligned}
 \frac{d}{dx} \sqrt{a^2 + x^2} &= \frac{x}{\sqrt{a^2 + x^2}} \\
 \frac{d^2}{dx^2} \sqrt{a^2 + x^2} &= \frac{1}{\sqrt{a^2 + x^2}} - \frac{x^2}{(a^2 + x^2)^{3/2}} \\
 \sqrt{a^2 + x^2} &= \frac{1}{\sqrt{a^2 + 0^2}} \cdot \frac{1}{2} x^2 + \mathcal{O}\left(\frac{x^4}{a^3}\right) \\
 &= \frac{x^2}{2a} + \mathcal{O}\left(\frac{x^4}{a^3}\right)
 \end{aligned}$$

$$\begin{aligned}
E_{\text{dst}}(x, y) &\approx \int_{\mathbb{R}^2} E_{\text{lens}}(x', y') \cdot A_{\text{lens}}(x', y') \\
&\cdot \exp\left(\frac{2\pi i}{\lambda} \left[\frac{(x-x')^2 + (y-y')^2}{2f} - \frac{x'^2 + y'^2}{2f} \right]\right) d\mathcal{L}(x', y') \\
&= \exp\left(\frac{2\pi i}{\lambda} \left[\frac{x^2 + y^2}{2f} \right]\right) \\
&\cdot \int_{\mathbb{R}^2} E_{\text{lens}}(x', y') \cdot A_{\text{lens}}(x', y') \cdot \exp\left(-\frac{2\pi i}{\lambda} \frac{xx' + yy'}{2f}\right) d\mathcal{L}(x', y') \quad (9)
\end{aligned}$$

From equation 9 it can be seen that the destination field is (up to a constant phase) approximately the Fourier transform of the light incident on the lens. This insight opens up a completely different approach to pattern generation. Instead of applying amplitude modulation to an incident beam one applies phase modulation and then performs a Fourier transform on the light field.

4.1.1 Influence of Pixel Structure

To analyze the behavior of a spatial light modulator it is instrumental to treat it as a grid of point sources which are individually modified. However, this treatment is only approximately correct. In this section I will present an extended formalism accounts for the non-vanishing size of the individual pixels.

The electric field distribution on the point source grid can be understood as a sum of delta distributions:

$$E_{\text{simple}}(x, y) = \sum_{j_x=1}^{N_x} \sum_{j_y=1}^{N_y} A(j_x, j_y) \exp(i\varphi(j_x, j_y)) \delta(x - d_x j_x, y - d_y j_y)$$

where N_x, N_y define the grid dimensions and d_x, d_y the corresponding lattice constants. The far-field behavior of such a grid can be computed using the Fourier transform. Due to the lattice-like structure of this function, the result is an angular distribution with periodicity angle of $\frac{\lambda}{N_x d_x}$ in x-direction and analogously in y-direction. To compute the light utilization efficiency, the single-slit behavior of the individual pixels need to be taken into account. This can be achieved by convolving the point grid electric field with a window function

$$\begin{aligned}
E_{\text{pix}}(x, y) &= E_{\text{simple}} * \text{Wnd} \\
\text{Wnd}(x, y) &= \begin{cases} 1 & |x| \leq \frac{dp_x}{2} \wedge |y| \leq \frac{dp_y}{2} \\ 0 & \text{otherwise} \end{cases}
\end{aligned}$$

where $dp_x \leq d_x$ and $dp_y \leq d_y$ are the size of an individual pixel in x and y direction. The Fourier transform of this field is the product of the old field's Fourier transform and a

new angular attenuation function, given by the Fourier transform of the window function

$$\begin{aligned} \mathcal{FT}[\text{Wnd}] (\theta_x) &= \text{Att} (\theta_x, \theta_y) \\ &= \text{sinc} \left(\frac{dp_x \theta_x}{\lambda} \right) \cdot \text{sinc} \left(\frac{dp_y \theta_y}{\lambda} \right) \\ \text{sinc} (x) &= \frac{\sin (x)}{x} \end{aligned}$$

As an example is provided for a pixel size and pixel distance of 20 μm and a wavelength of 852 nm. The Fourier transfer function for the grating part is seen in figure 10. The far field of the single pixels is shown in figure 11. It can be seen that exactly at the secondary diffraction maxima of the grating the single pixel transfer function vanishes. Thus the far field distribution of the pixel suppresses the secondary maxima, as seen in figure 12. However, the fill factor in a spatial light modulator is usually less than 100%. In this case, the pixel width is smaller than the distance of the centers. If the pixel is narrowed, the Fourier space transfer function widens and the secondary maxima are not perfectly canceled out. For example, when the pixel width is reduced to 18 μm , the total transfer function changes from the one seen in figure 12 to the one in figure 13. It is instrumental to analyze the quantitative shape of the single-pixel transfer function further. The transfer function of the point source grid is what is modified by setting the pixel-by-pixel phase, but the single-pixel part of the transfer function remains fixed.

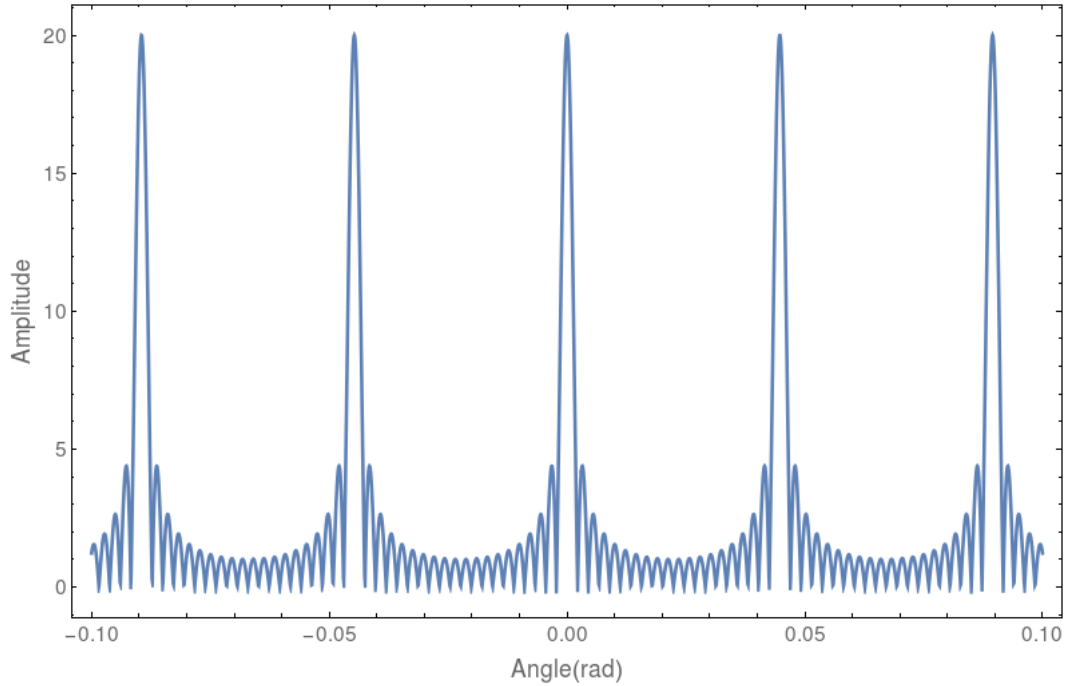


Figure 10: Far field distribution of a 20 point grating

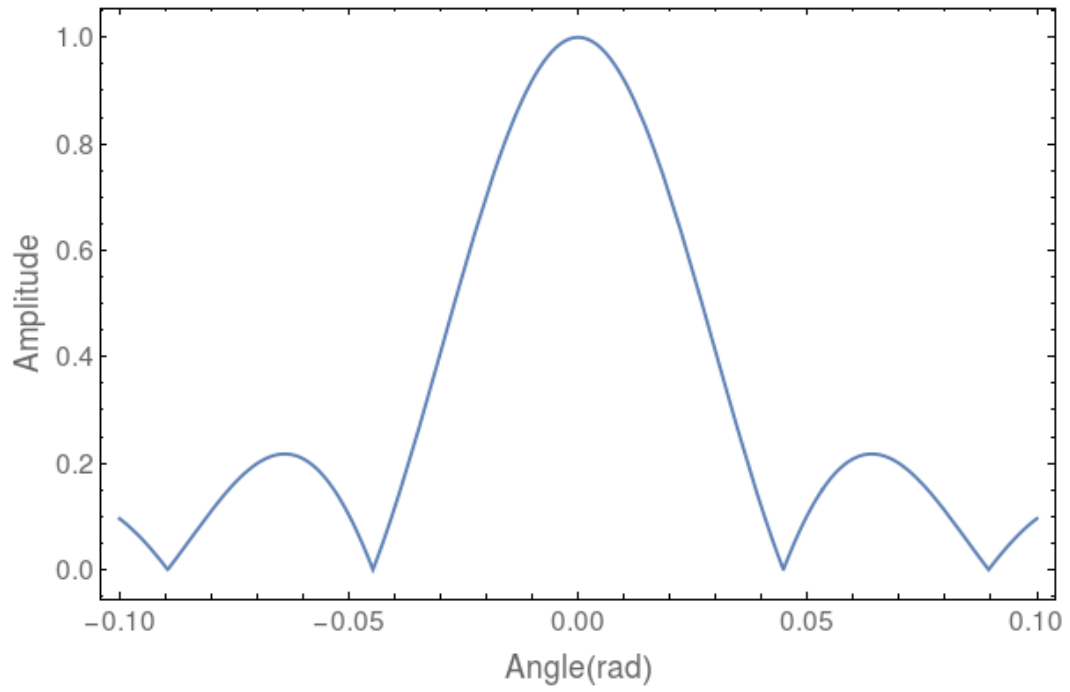


Figure 11: Far field distribution of a single 20 μm -pixel

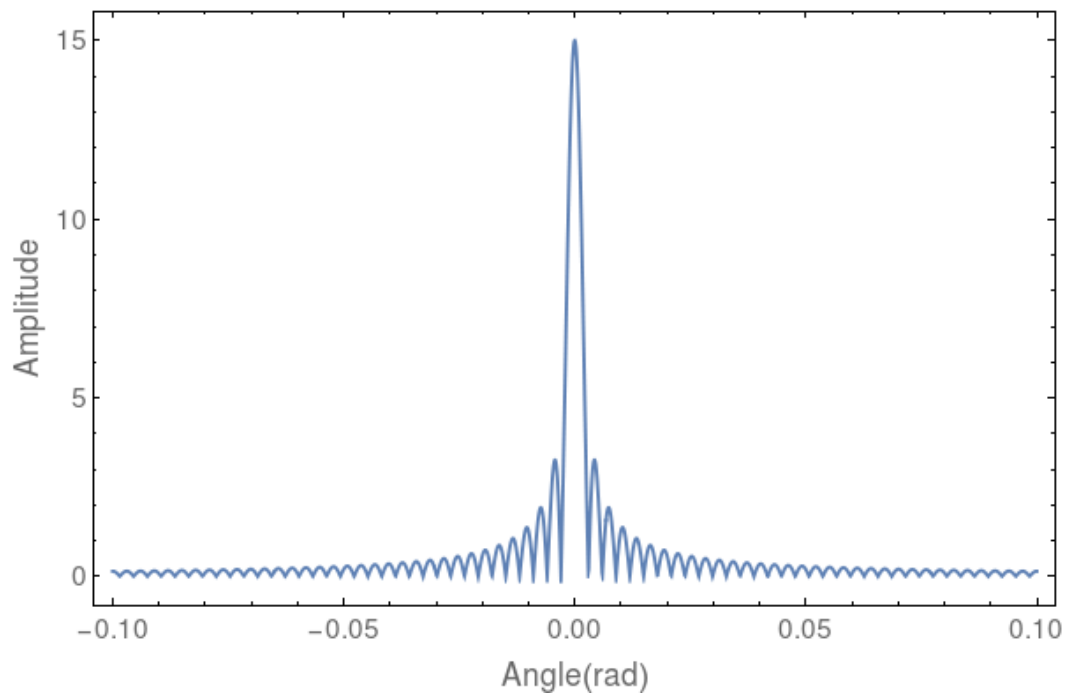


Figure 12: Far field distribution for a grating of 20 $20 \mu\text{m}$ pixels with a center-to-center distance of $20 \mu\text{m}$

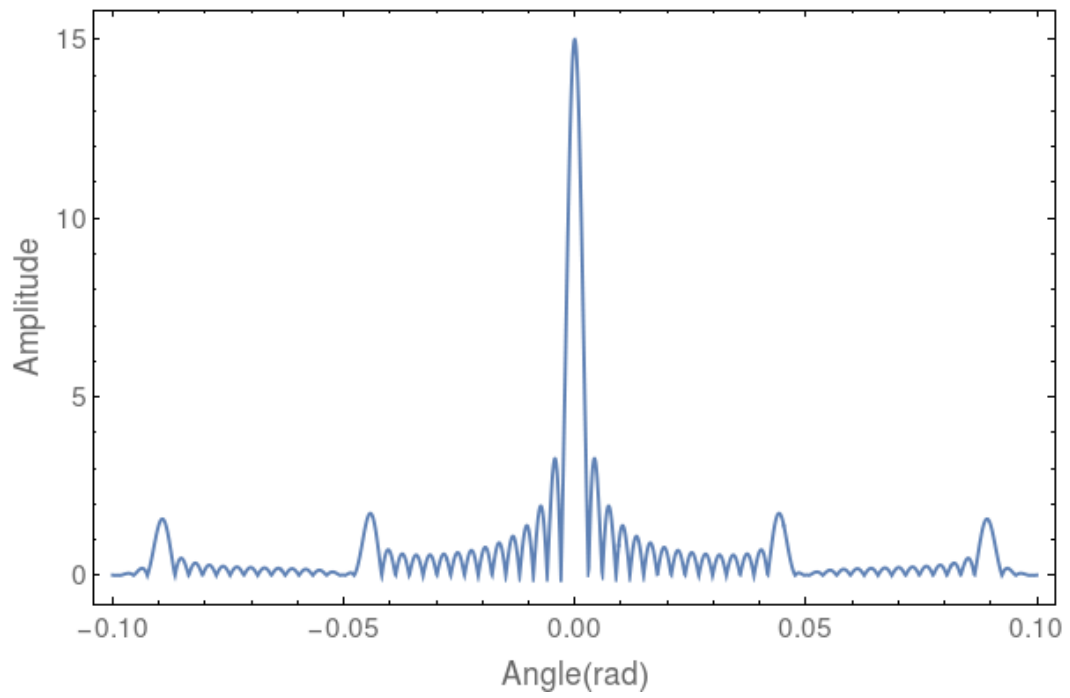


Figure 13: Far field distribution for a grating of 20 $18 \mu\text{m}$ pixels spaced at $2\mu\text{m}$ distance

4.2 The Gerchberg-Saxton Algorithm for Phase Pattern Computation

The problem of phase computation is a non-local (due to the Fourier transform) and stiff (since all Eigenvalues of the Fourier transform have magnitude 1) non-linear (due to the exponential map $e^{i\cdot}$ from phase to field) problem. The combination of Fourier transform and exponential map is bijective (mod 2π in phase), however the input and output amplitudes are constrained while only the phases can be varied freely. This problem can be significantly relaxed by allowing image amplitude to vary outside of a defined region of interest. The underlying algorithm used in this thesis has been first presented in [12]. It constitutes an iterative approach to approximate the destination amplitude distribution. It will be discussed with the following terminology:

- *Source plane* - The plane in which the modulator resides. The phase in this plane can be varied, the amplitude distribution is fixed by the incident intensity distribution. The final phase in this plane is the algorithm's output.
- *Destination plane* - The plane in which the desired image is to be projected. In this plane the amplitude distribution is fixed in the region of interest and can be varied outside. The phase can be freely varied everywhere.

The steps of the algorithm are detailed in algorithm 1. Alternatively consult figure 14 for a schematic overview. A proof of convergence is shown in [12].

4.3 Minor Modifications of the Algorithm

Oscillation Control

In order to prevent oscillations of the algorithm, step 3 was replaced by the following alternative step:

- Set $E \leftarrow \frac{E}{|E|} \cdot [\lambda A + (1 - \lambda) |E|]$ where $\lambda \in [0, 1]$ is a step regularization constant

Adaptive Oversteering

One consistent problem of this algorithm was that it failed to properly converge in some areas of the destination plane. In order to improve this behavior, a method to systematically oversteer the destination amplitudes was developed. This modification can be thought of as adding an integral controller to the algorithm's main loop. This was achieved by replacing step 3 with the following steps:

1. Adapt moving amplitude target by $M \leftarrow M + \alpha (A - |E|)$ where M is the moving amplitude target, A is the true desired amplitude target, $|E|$ is the destination plane field amplitude in the current step and α is a small integration constant.
2. Set $E \leftarrow \frac{E}{|E|} \cdot M$ or $E \leftarrow \frac{E}{|E|} \cdot [\lambda M + (1 - \lambda) |E|]$ (whether you want to use the technique outlined in section 4.3).

The moving amplitude target is initialized with $M \leftarrow A$ so that it matches the amplitude target.

Algorithm 1 Gerchberg-Saxton Algorithm for Phase Map Computation[12]

Variables & Parameters:

- E (variable): Current complex scalar field in either source or destination plane
- A (parameter): Desired amplitude distribution in the destination plane
- A' (parameter): Given amplitude distribution in the source plane (by input beam shape and objective aperture)
- P (return value): Phase distribution of the source plane field that satisfies amplitude constraint in source plane and approximately in destination plane

Execution steps:

1. Define complex scalar source plane field E using initial random phase and predefined intensity distribution (obtained from measurement).
 2. Transform E from source plane to destination plane field via Fourier transform.
 3. Set $E \leftarrow \frac{E}{|E|} \cdot A$, where A is the intended amplitude distribution in destination plane (Retain phase and modify amplitude).
 4. Transform E from destination plane to source plane via inverse Fourier transform.
 5. Set $E \leftarrow \frac{E}{|E|} \cdot A'$, where A' is given by source amplitude distribution (the same as it was initialized with)
 6. Transform E from source plane to destination plane field via Fourier transform.
 7. Check for convergence. If acceptable, continue at 8. Otherwise, continue at 3.
 8. Transform from destination plane to source plane field via inverse fourier transform.
 9. Extract phase P from source plane field E .
-

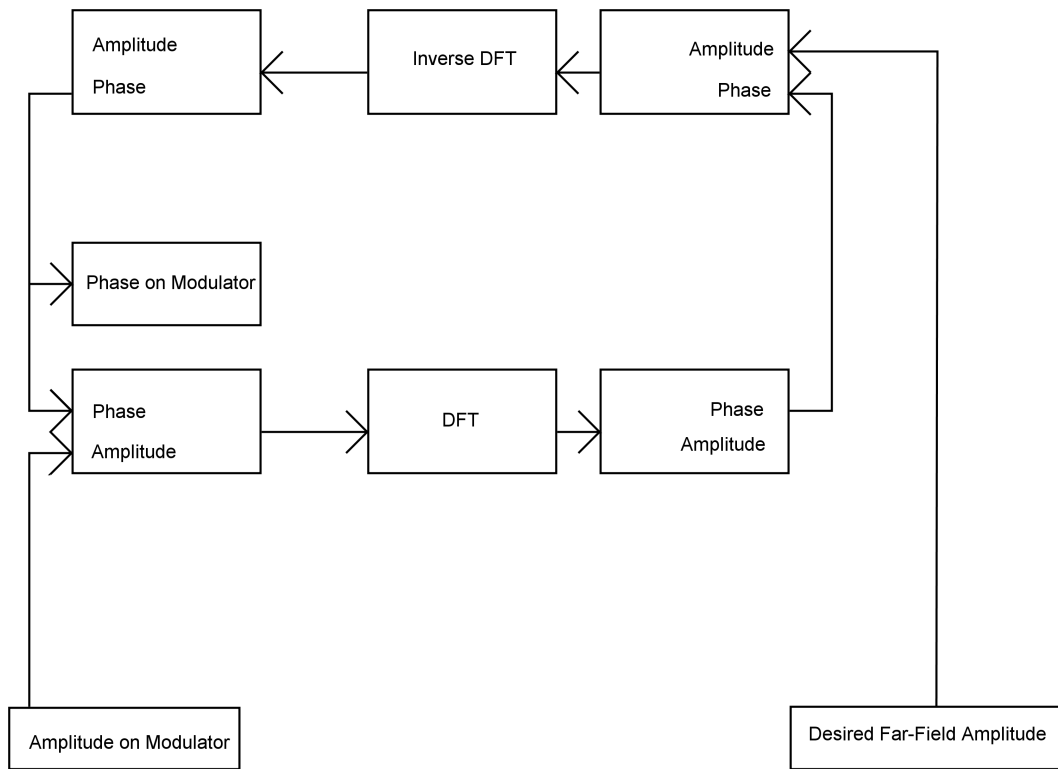


Figure 14: Graphic schematic of the Gerchberg-Saxton algorithm ([12])

Treatment of Vanishing Fields in the Destination Plane

When during the execution of the algorithm, the field amplitude in the destination plane vanishes in a single step, the Fourier transform can form phase vortices (where the phase performs a full 2π rotation around a central point) both around this point in the destination plane, as well as in the source plane. Because these phase vortices are non-local and in complex geometries hard to detect, they are stable between iterations and can cause speckles in the image which are near impossible to remove in this iterative algorithm (although phase vortex distortions can move that point). Because of this, it is instrumental to immediately eliminate vanishing field amplitudes when they are encountered (as long as the desired amplitude is nonzero, if it is intended to vanish, then the vortices can help stabilize this requirement). In this implementation this is simply performed by assigning the destination field a nonzero amplitude (the moving target amplitude whenever it is nonzero) and a randomly chosen phase.

4.4 The Problem of Optical Phase Vortices

The Fourier transform represents an evolution of the field along the optical axis from the source to the destination plane. The phase winding number around any closed path in the image is a conserved quantity of this evolution [28]. However, every phase winding must contain a point of discontinuous phase at its interior. To preserve continuity of the field, the amplitude has to be exactly zero at this vertex. Since the phases are preserved by the Gerchberg-Saxton iterations, the algorithm is not able to explicitly eliminate these vortices. It can, however, annihilate vortices of opposite phase winding close to each other during the Fourier transform step. The converse of this is in principle also possible - a pair of oppositely wound vortices can be created from regions of strong phase fluctuation, however the creation and separation of stable vortices is unlikely. In order to eliminate vortices, it is possible to decompose the field into a real-valued amplitude, a vortex-free phase-component and a component containing the phase vortices [28]. Then, the first two components can be used to create a vortex-free approximation to the previous field. Alternatively, the vortex component can be used to determine the location of vortices, and vortices deemed especially problematic (e.g. in high amplitude regions) can be eliminated by putting a vortex of opposite winding on top and letting the two vortices annihilate to multiple iterations. This would present the benefit of having a smaller overall impact on the phase distributions, which makes this option more attractive in later stages of the algorithm's execution.

4.5 Alternative Algorithm Optimized for Optical Tweezers

While the Gerchberg-Saxton iteration scheme produces a compromise between image sharpness and light utilization efficiency, it requires a large amount of computation time. If only a few lattice sites need to be illuminated and light utilization efficiency is not of paramount importance, then an alternative scheme can be used.

For each site to be illuminated, a grating pattern P_j is computed that diffracts all light into the destination site. Then each modulator pixel is assigned randomly (or pseudo-randomly using the intensity distribution on the modulator) to one of the patterns, and takes its phase from the corresponding pixel on that phase pattern. Each site receives a

power of

$$P_j = P_{\text{tot}} \frac{\left(\sum_{x \in S_j} \text{Amp}(x)\right)^2}{|S| \sum_{x \in S} (\text{Amp}(x))^2}$$

where S_j is the set of pixels assigned to site j , S is the set of all pixels on the modulator, and $\text{Amp}(x) : S \rightarrow \mathbb{R}^+$ is the mapping from pixels to their amplitudes. This formula assumes constructive interference of all pixels assigned to a single destination site. It is derived from the proportionality of power and squared amplitude as well as the symmetric form of the discrete Fourier transform ($\mathcal{DFT}^{(-1)}[u]_k = \frac{1}{|u|} \sum_{j=0}^{|u|-1} e^{\pm 2\pi i \frac{kj}{|u|}}$). Assuming n equally brightly illuminated sites one gets an expected power per target site of:

$$\frac{P_j}{P_{\text{tot}}} = \frac{1}{n^2}$$

This means that the remaining power share of $1 - \frac{1}{n}$ is distributed pseudo-randomly across all other lattice sites.

4.5.1 Performance Analysis for 100 Tweezers

In order to determine the image quality, the discrete Fourier transform of a circular aperture was analyzed. This analysis was performed once for the the whole aperture as a reference and once for a set of 1% of randomly chosen sub-pixels.

In order to properly review the point-spread-function in Fourier space, the circular aperture was padded with a mask to increase the input image size by a factor of 10 (which also enhances the resolution in Fourier space by the same factor). Since the amplitude is lowered by a factor of $(100)^{-1}$ in the sub-sampling approach, all amplitudes were normalized to the maximum amplitude to review shape and amplitude distribution of the point-spread-function correctly. Review of figure 16 shows virtually no visual difference in shape between the two point-spread-functions. The white dots in the figure are markers for lattice site positions in x direction to convey the 10x super-sampling. This hints that loss of light utilization efficiency might be the only serious problem of this scheme. However, this property needs to be tested experimentally to be verified.

Beyond qualitative analysis, I also analyzed the amplitude distributions in form of histograms. Two properties of interest are the histogram of amplitudes in the upper amplitude range to ensure that no additional high-amplitude spots are created by accident (see figure 17) as well as the total amplitude histogram in the point spread function window shown in figure 16 (see figure 18). Both histograms show an extremely high degree of similarity in quantitative brightness distribution. The only significant deviation can be seen in figure 18 in the low-amplitude-region. I do not expect this difference to lead to a critical problem in practice.

5 Implementing Inline Holography for the Two-Dimensional Quantum Walk Experiment

5.1 The Optical Layout

The optical lattice is in the focal plane of the Two-Dimensional Quantum Walk system's imaging objective (its Fourier plane). In order to create an intensity pattern on the lattice,

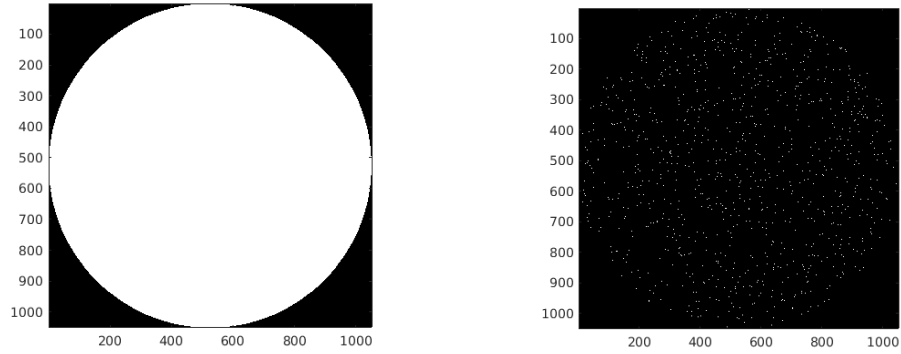


Figure 15: Full aperture (padding not shown) and sub-sampled region

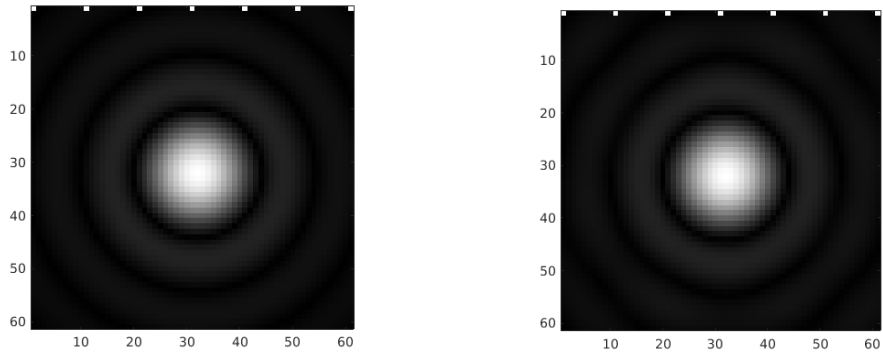


Figure 16: Point spread function around a single Fourier mode - full aperture (left) and sub-sampled (right) - images separately normalized to maximum value

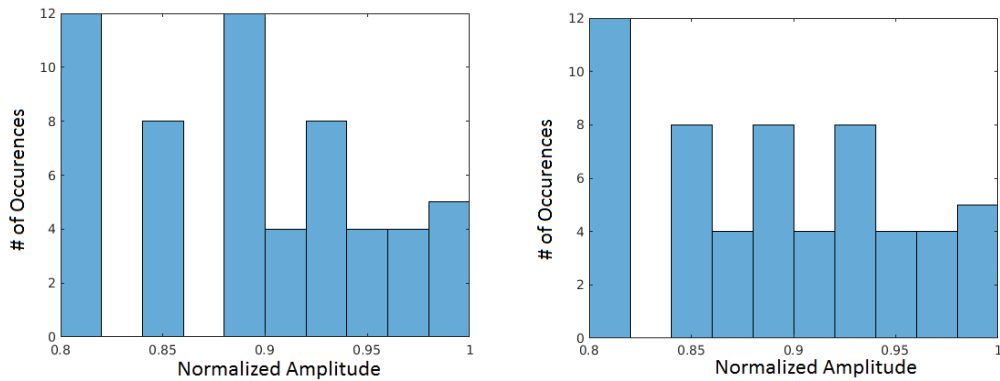


Figure 17: Histogram of normalized amplitudes (limited to upper 80% of amplitude) for full aperture (left) and sub-sampled (right)

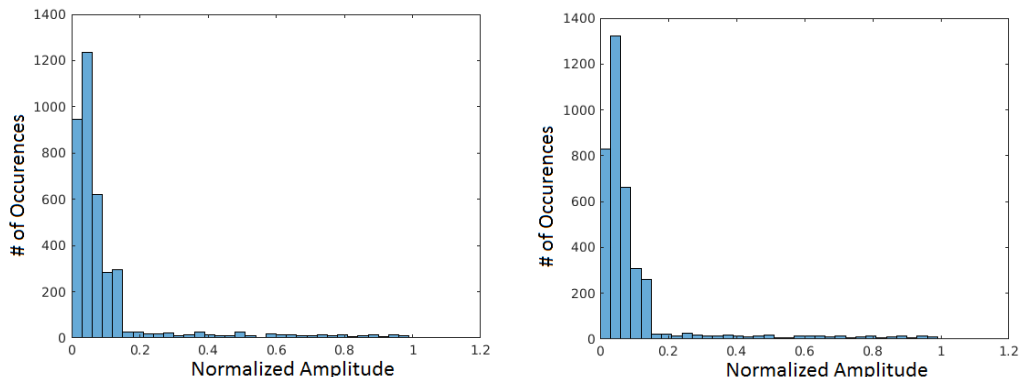


Figure 18: Histogram of normalized amplitudes over the window in figure 16 for full aperture (left) and sub-sampled (right)

the phase pattern on the modulator needs to be imaged onto the objective. Since the modulator and objective are of different diameters (Objective: 22 mm, Modulator: 18.6 mm) the beam widths need to be matched using a telescope. Additionally, the fiber's output beam needs to be matched to the size of the modulator. Another challenge when imaging the modulator is its 0th diffraction order. Even though it only makes up a small share of the light (at a 96% nominal light utilization efficiency) the objective focuses it into a single point on the destination plane. This means that this component needs to be blocked or redirected.

The core of the imaging systems is a 3-way T-shaped telescope with focal length ratio 20mm : 150mm : 300mm. At the center of the T resides a rectangular prism mirror (see fig. 20), which is coated up to and including the 90° edge. The intermediate focal plane of this telescope contains the image to be projected onto the atoms in the optical lattice. By placing the edge right inside or close to this plane, one can cut the intermediate image in half, directing one half towards the atoms and the other half (which at proper edge placement contains the 0th order) back through the 20mm arm. In this configuration, the separated image is still within 0.02° of the single pixel transfer function maximum (see section 4.1.1). Additionally, This design minimizes the angle of the modulator and integrates two telescopes into a compact arrangement.

In order to ensure that all components are well aligned with respect to each other, the central prism mirror, the lenses and the modulator were placed in an optomechanical 60mm cage. While the lenses can be mounted using standard cage mounts, the prism mirror and the modulator required different mounts. I decided to mount both the modulator and the central prism mount on a compact 5-axis stage (3 translation, 2 rotation) to help with proper alignment. The prism mirror was clamped onto the stage for the test setup (when putting it into the setup it needs to be glued on since the setup is on a vertical plane), while I designed a custom mount for the modulator. The stages are connected both to the ground and to the cage using a custom-designed connector.

An overview of the whole testbed setup is shown in figure 21. Note that this is not the current iteration of the setup but an older one where the component placement around the imaging system has a simpler structure. The blue box represents the section intended to be taken into the laboratory. The leftmost part contains the laser source (diode laser in

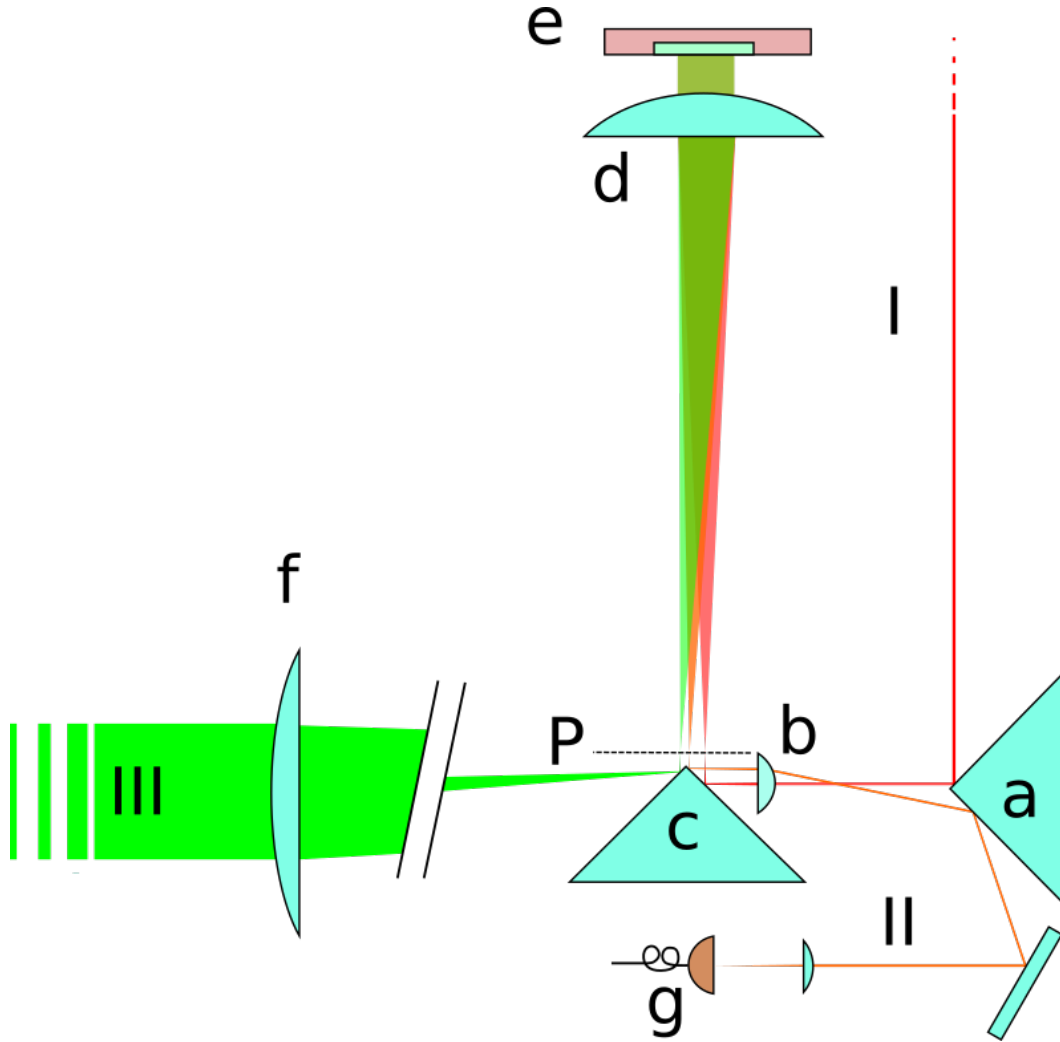


Figure 19: Schematic of the whole telescope - The incoming polarized light (I) is imaged via two prism mirrors (a, c) and the 20mm lens (b) through the intermediate focal plane (P) and via the 100mm lens (d) onto the SLM (e). The first order reflection (II) is separated from the image in the focal plane P and split off at the prism edge (c). It is then guided via (b) and (a) onto a photodiode (g) to be taken as an intensity reference. The image points (III) are split off from beams (I) and (II) via (c) and collimated using a 200mm lens (f). The collimated beams are then directed to the objective.

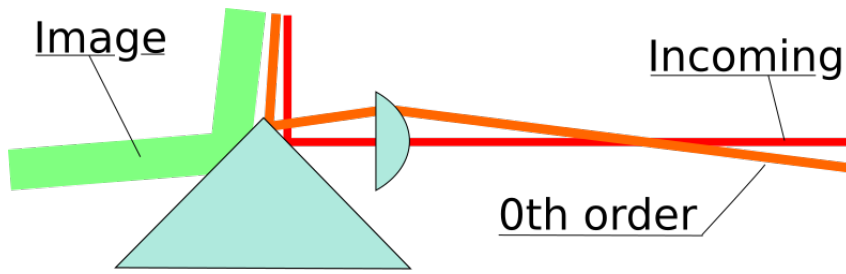


Figure 20: Zoomed view to the 3-way mirror telescope. The black box represents the lens tube holding the 20mm telescope lens.

Littrow configuration, 852nm) as well as an optical isolator and a fiber incoupler. In the version shown here, which had shorter focal length imaging lenses, the beam was initially magnified to cover the whole modulator. Since the focal lengths of the 2" diameter lenses are now increased, this initial magnification is no longer necessary. The orange path can be used as a reference for intensity stabilization and laser locking. In the testbed it was not needed and simply blocked. The green beam leaves the telescope collimated and is focused onto the photodiode. The green beam is directed onto a photodiode for calibration. For taking images a camera is placed next to the photodiode and the beam redirected using the mirrors. The role of the objective is here taken by the focusing lens in front of the last mirror. Note that this older version of the setup does not feature a pinhole in front of the photodiode. This was added in a later stage.

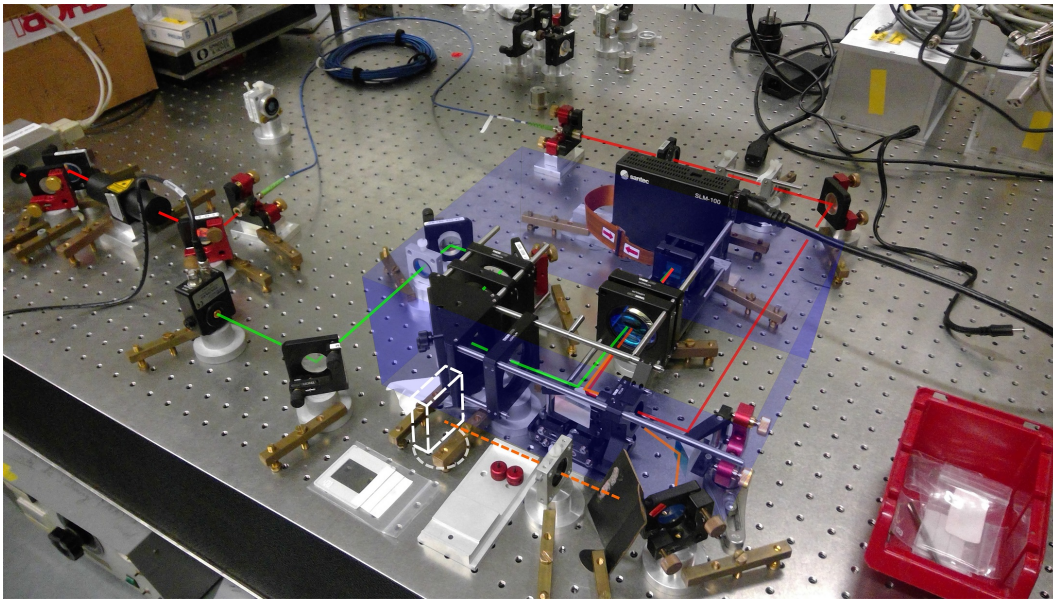


Figure 21: Overview of a past version of the physical setup showing the beam paths

5.1.1 Lens Configurations

For the secondary telescope to properly image the modulator onto the objective, the distance between modulator and first lens d_1 and the distance between the second lens and the objective d_2 must satisfy

$$\begin{aligned}d_2 &= \left(1 + \frac{f_2}{f_1}\right) f_2 - \left(\frac{f_2}{f_1}\right)^2 d_1 \\ &= (1 + M) f_2 - M^2 d_1\end{aligned}$$

For analysis and image evaluation two different configurations were selected

- **Laboratory-Friendly Configuration:** $d_1 = 10$ cm, $d_2 = 50$ cm. This configuration was chosen as an example for the intended setup in the experimental laboratory. Due to existing constraints in the experiment, the objective lens needs to be placed far away from the imaging system.
- **$2f + 2f$ Configuration:** $d_1 = f_1 = 15$ cm, $d_2 = f_2 = 30$ cm. This configuration was selected because of the good aberration suppression of $4f$ -imaging systems.

5.2 Simulated Imaging Performance

In order to determine the expected aberrations caused by the imaging layout, the setup was simulated using the OSLO software package developed by Lambda Research. The optical path lengths are then computed as the lengths of a ray traced from a far away source point to the intersection point with the imaging surface. The assumptions concerning the lens parts can be seen in table 1. All lenses are planar-convex lenses.

Placement	Curvature radius	Center thickness	Diameter	Back focal length	Model
b	10.3 mm	4.0 mm	1/2"	17.3 mm	ThorLabs LA1074-B
d	77.3 mm	7.3 mm	2"	144.7 mm	ThorLabs LA1417-B
f	154.5 mm	5.1 mm	2"	295.6 mm	ThorLabs LA1256-B

Table 1: Lens data for OSLO simulation (see fig. 19 for placement)

Property	Value
Width	14.98 mm
Height	10.92 mm
Diagonal	18.54 mm
Pixel size	10 μm
Pixel pitch	10.4 μm

Table 2: Geometric reference data Santec SLM-100

Input to Modulator

The telescope imaging the input beam onto the modulator has a magnification factor of $M_{\text{in}} = 7.5$. A beam of diameter 2.5 mm is magnified to a 18.75 mm wide beam. Since the modulator has a diagonal of 18.54 mm this input diameter is sufficiently large. This ray-tracing calculation was performed operating the program in afocal mode. In this mode, the image plane used to compute optical path length distances is a large spherical surface centered around the intersection between the last lens surface and the optical axis. The field angle was set to the minimal possible value of $5 \cdot 10^{-5}$ since the imaging of this system is collimated beam \leftrightarrow collimated beam. During analysis a defocus was found. It was corrected by separating the lenses by an additional 2.3 mm. After this correction the maximum optical path length difference is 0.238 λ incident on the modulator (see fig. 22).

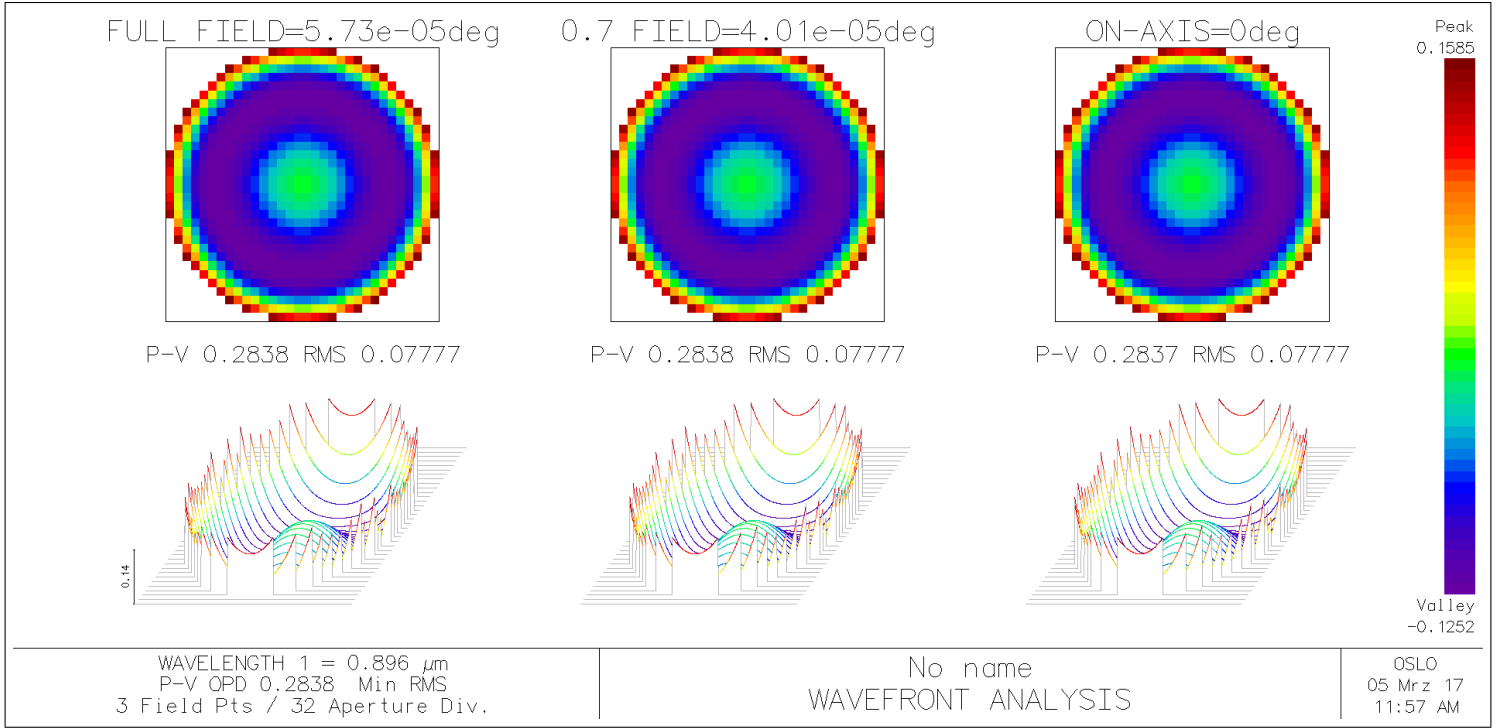


Figure 22: Input-to-modulator telescope waveform distortions (after defocus correction)

Modulator (Collimated) to Output (Collimated) in Far-Objective Configuration

In this analysis the distortions of collimated wavefronts emitted by the modulator are calculated. The imaging setup was set up in far objective configuration (see section 5.1.1). The absolute maximum diffraction angle of the Santec SLM is given by the ratio between the wavelength and the pixel size $\frac{\lambda}{d_{\text{pix}}} = \frac{895\text{nm}}{10\ \mu\text{m}} = 90\ \text{mrad} = 5.1^\circ$. At this diffraction angle is the first minimum of the pixel transfer function. However, the image should only be placed around the maximum of the transfer function. Since at an angle of 0.02° the image is already separated well from the 0th order, assuming a maximum diffraction angle of 1° seems a reasonably conservative assumption. The modulator's smallest cross section (which is the height of 10.92 mm) is used as the beam diameter. A graphical overview of an afocal analysis can be seen in figure 23. After applying the a defocus correction as above - this time with an additional distance of 6.5 mm , the results of the analysis can be seen in figure 24. On axis, the waveform distortions are as small as 0.06λ while even at 70% field angle they are still below $\frac{\lambda}{4}$. Since the patterns will be of angular size of around 0.5° , this is already acceptable value for testing (the distortions are mainly at the border which are not imaged).

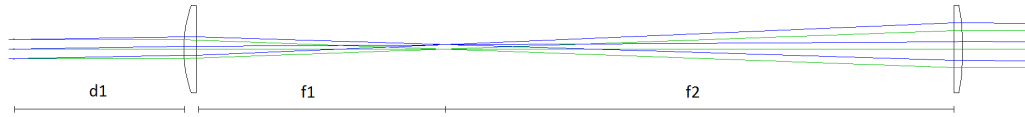


Figure 23: Modulator to objective imaging system - structure of simulation

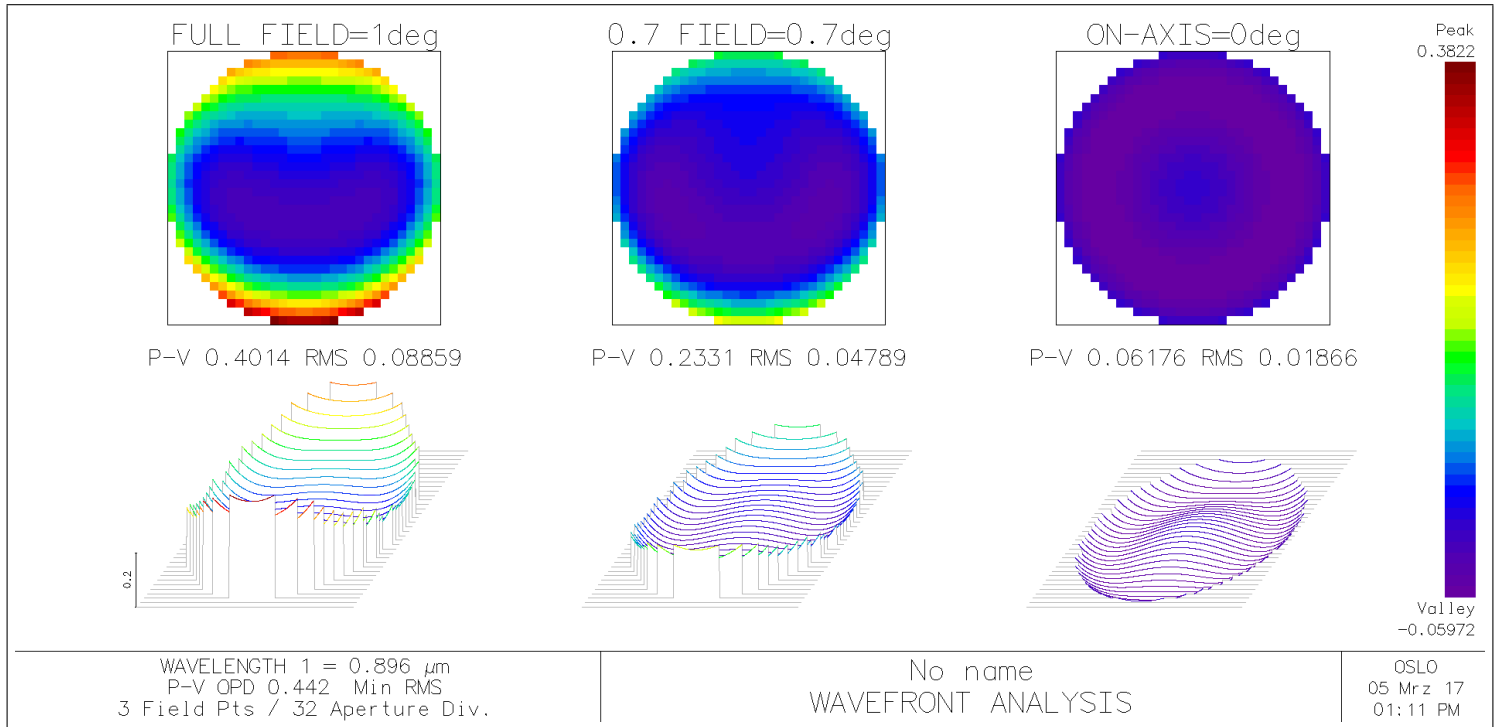


Figure 24: Modulator-to-output telescope afocal waveform distortions (after defocus correction)

Modulator Plane to Objective Plane in Far-Objective Configuration

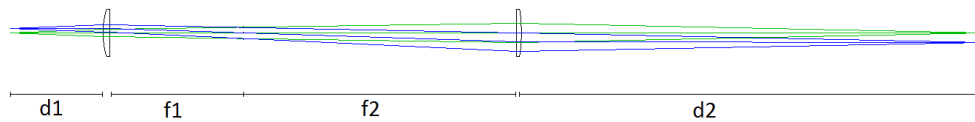


Figure 25: Setup view of the modulator-to-objective calculation

In a second analysis, the transfer of individual pixels is analyzed (see figure 25). Here each wavefront angle corresponds to a location of the modulator being imaged, while the

wavefront distortion is plotted over the possible paths that the light could take through the input aperture of the system at angles of $\pm 4^\circ$. To model this, the aperture stop was placed in the intermediate image plane at a radius of 6 mm.

When performing this focal analysis (modulator point to objective), the results seen in figure 26 do provide a similar picture. The central pixel (see figure 26 section “On-Axis”) as well as the rays passing through the center of the intermediate image acquire not enough optical path length differences for destructive interference. However, there are still aberrations of order 0.1 – 0.2 wavelengths to suppress.

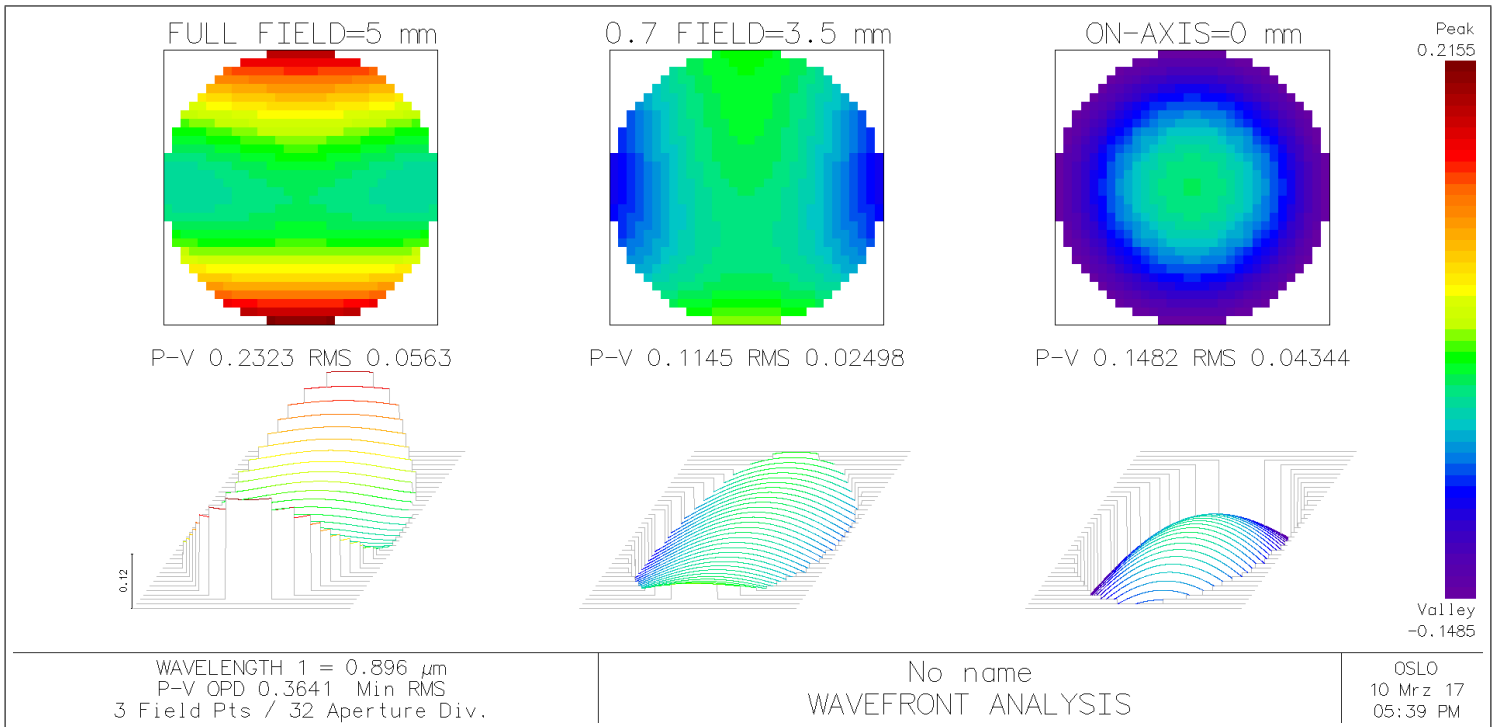


Figure 26: Modulator-to-output telescope afocal waveform distortions (after defocus correction)

Modulator Plane to Objective Plane in $2f + 2f$ -Configuration

As a comparison the same analysis as above was also performed in $2f + 2f$ -configuration (see section 5.1.1). The results in figure 27 show a similar performance compared to the far-objective configuration at high field angles (which correspond to far off-center modulator pixels). However, an improvement by a factor of 3 can be seen at low field angles.

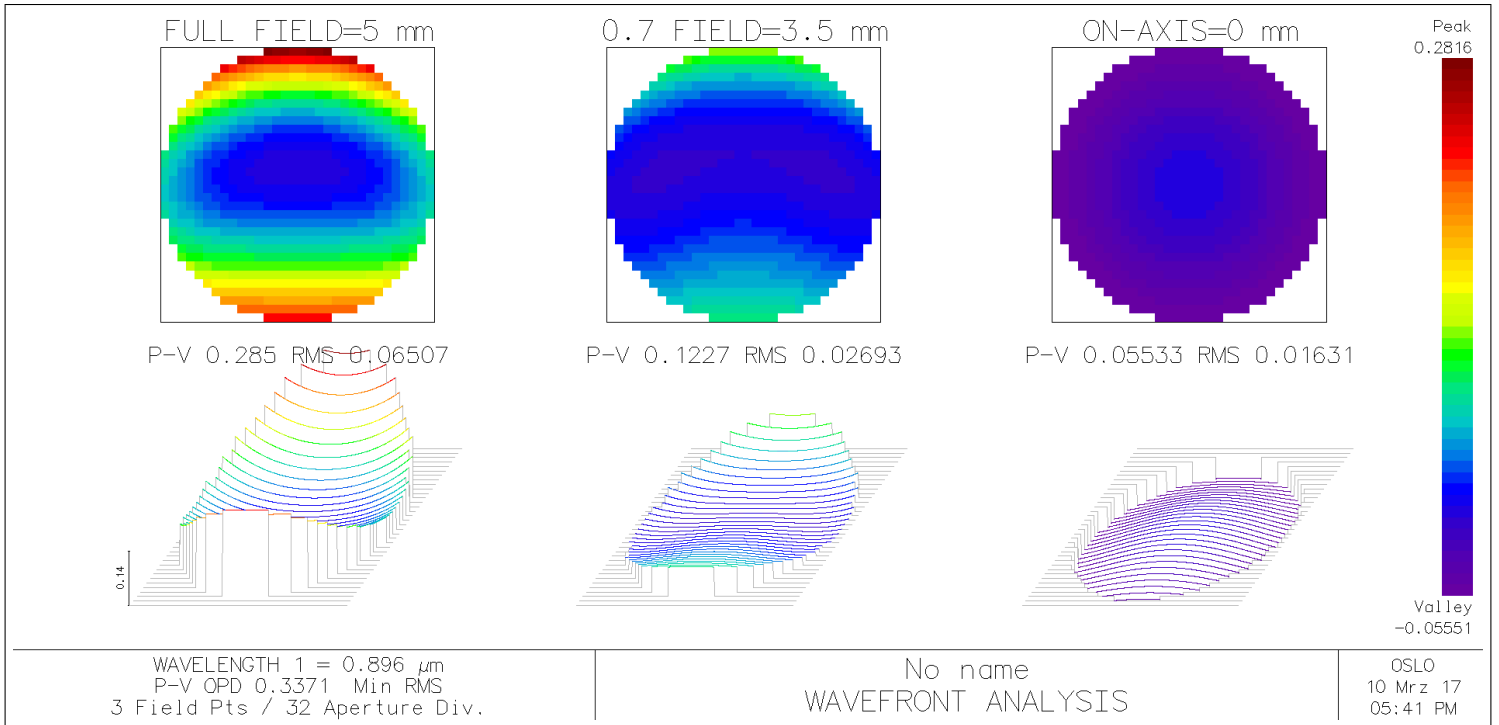


Figure 27: Modulator-to-output telescope afocal waveform distortions (after defocus correction)

Input (Collimated) to Output (Collimated) in Far-Objective Configuration with Distance Adjustment

For completeness also the imaging performance of the optical layout was computed. For this computation the evolution of collimated beam wavefronts through both telescopes was analyzed. A beam diameter of 2.5 mm was used as an input for the simulation. All lens distances were the sums of the back focal lengths. The modulator (here understood as a simple mirror) was placed at a distance of 10 mm from its imaging lens. The lens distances between input- and modulator- as well as modulator- and output-lens were varied identically. The optimal aberration suppression in simulation was found at an additional offset distance of 4.15 ± 0.02 mm between all lenses. The results of the aberration computation can be seen in figure 28.

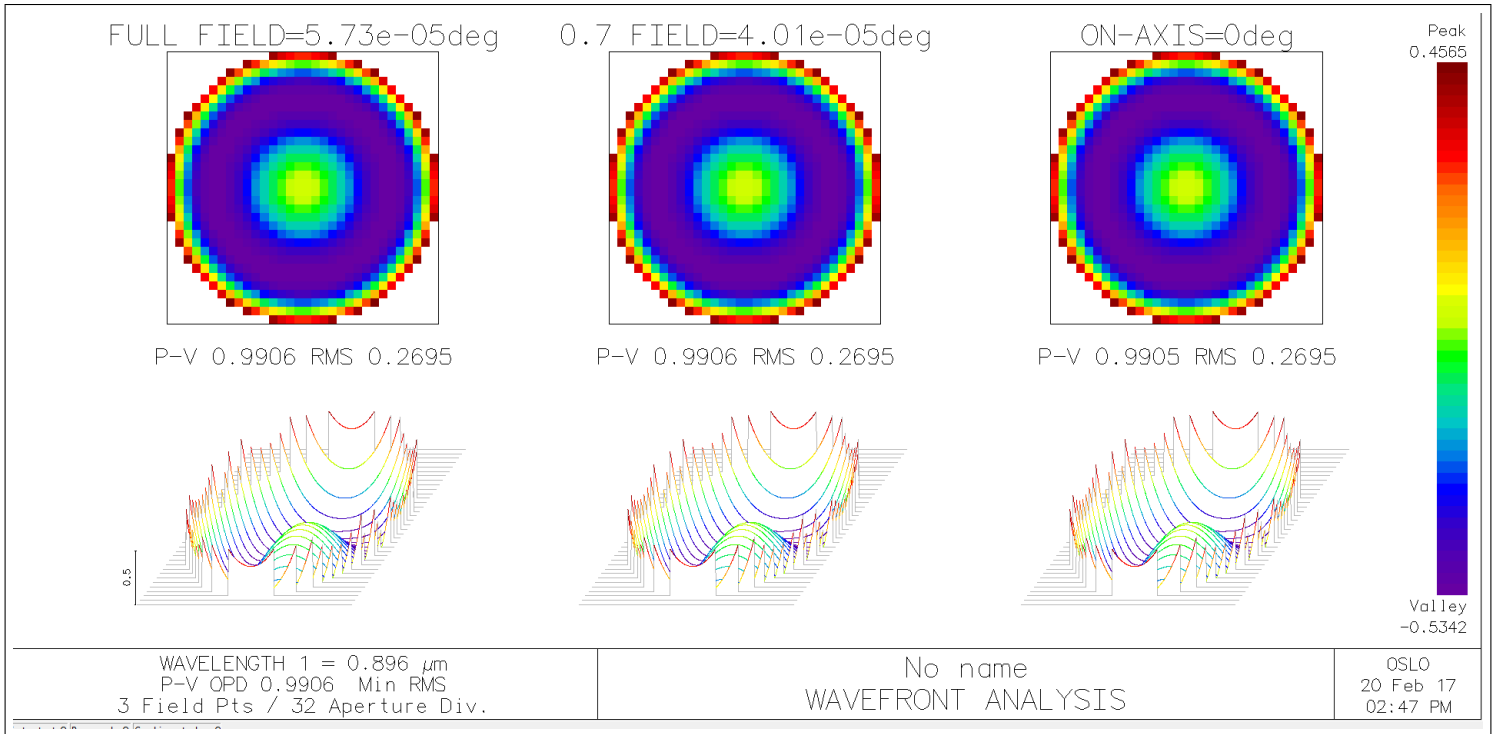


Figure 28: Aberration simulation of the imaging setup (without objective) with defocus correction

5.3 Calibration of the Spatial Light Modulator

There are three unknowns which need to be determined during calibration:

- Phase gain coefficient (or alternatively, the wavelength at which the devices provides a phase hub over exactly the $[0, 2\pi)$ range, from now on called the *device wavelength*)
- Phase deformations on the modulator (which can be caused by imaging aberrations, beam phase distortions and geometrical distortion of the modulator)
- Intensity / amplitude distribution on the modulator (primarily induced by beam-shape and the objective's optical aperture)

The calibration is performed by focusing the collimated image beam using a placeholder objective and placing a photodiode in the focal plane. To increase spatial accuracy of the calibration, a 200 μm pinhole is placed in front of the photodiode.

Pre-Calibration alignment

The mirror edge separating arms paths II and III (see fig. 19) is placed at a small ($\leq 0.02^\circ$) angle from the 0th order (mirror-like) reflected beam to separate the two arms. Without phase modulation all light is reflected into arm II instead of arm III where the photodiode is placed. To diffract light into the image arm an angled diffraction grating is displayed on the modulator. This diffraction grating is implemented by putting a linear phase ramp in x direction onto the modulator area. Restricting the phase hub levels to a $[0, 2\pi]$ range transforms the linear ramp into a sawtooth pattern.

5.3.1 Linear Phase Gain

In order to determine the phase gain, I added a variable checkerboard pattern onto the base phase grating. Every even pixel (as in $x + y$ even) had its phase unmodified, while the phase on all odd pixels was uniformly varied. Varying the phase $\Delta\varphi$ of the odd pixels (with respect to the light wavelength) from 0 to 2π , one would ideally expect the response form

$$\begin{aligned} V &\propto I \\ &\propto |E|^2 \\ &\propto |1 + e^{i\Delta\varphi}|^2 \\ &= 2 + 2 \cos(\Delta\varphi) \end{aligned}$$

Taking into account offset and proportionality between intensity and voltage, one can fit an expression of the form $V(\Delta\varphi) = V_0 + V_c \cdot \cos(\varphi_0 + \alpha\Delta\varphi)$. If the modulator is already properly calibrated (meaning that the phases applied to the light are as predicted) then one would expect a result $\alpha = 1$. If $\alpha \neq 1$, one can adjust the device wavelength $\lambda_D \rightarrow \alpha\lambda_D$ to compensate for the deviation. Since the manufacturer-supplied device wavelength was found to be accurate within $< 1\%$ ($|\alpha - 1| < 0.01$) this adjustment was deemed unnecessary.

5.3.2 Beam Profile and Objective Aperture

The simplest incident light distribution for holographic calculation is the perfect flat top beam - a uniform light field over the whole modulator in intensity and phase. In practice,

this is hard to achieve. If the modulator is illuminated using a Gaussian beam, there is always a trade-off to be made between intensity flatness and power efficiency, since the inhomogenous flanks still contain significant power. Additionally, while being the simplest distribution, it is not guaranteed to be the optimal one, as the optimal distribution would be the one matching an inverse Fourier transform of the desired image - where the phases can be freely chosen. However, no matter the shape of the distribution, it is important that this shape is *known*.

The intensity distribution on the modulator is determined by walking a small patch of diffraction grating over the SLM and imaging the first diffraction order onto a photodiode. The photodiode then gives a response in linear relation to the diffracted power. The amplitude is then proportional to the square root of the power density

$$A(V) \propto \sqrt{V - V_0}$$

where V_0 is the background voltage of the photodiode, determined by removing the diffraction grating patch completely. Choosing the correct patch size is a tradeoff between signal-to-noise ratio and spatial resolution. A big patch size will provide a strong signal, while also low-pass filtering the intensity distribution. A smaller patch, while giving a better spatial resolution, might decrease the signal-to-noise ratio to a degree that the fitting calculations in section 5.3.3 might fail – although one can improve in this area by taking more measurement points.

5.3.3 Phase Distortions

The phase distortions can be determined by a technique similar to the one described in 5.3.2. Instead of just observing the light diffracted by a single patch, the interference fringe between an analyzer patch and a reference patch is recorded. The reference patch is preselected and kept stationary while the analyzer patch is walked over the modulator and has its phase hub modified. When traveling from the laser source to the sensor, the light paths going via the two patches pick up a phase difference φ_0 . To measure this phase difference the phase on the target patch is varied by adding a phase modulation of $\Delta\varphi$ while the reference patch is left unchanged. When modulating the phase, an interference fringe can be observed on the photodiode:

$$\begin{aligned} V(\Delta\varphi) - V_0 &\propto I \\ &\propto A^2 \\ &\propto \left| A_1 + A_2 e^{i(\varphi_0 + \Delta\varphi)} \right|^2 \\ &= A_1^2 + A_2^2 + 2A_1A_2 \cos(\varphi_0 + \Delta\varphi) \end{aligned} \tag{10}$$

where A_1 and A_2 are the light amplitudes associated to the reference and analyzer patch respectively. Fitting the fringe using equation 10 produces the phase difference φ_0 between the analyzed and the reference patch. Care needs to be taken in case the analyzed patch and the reference patch overlap. The first solution I tried was to (in this case) use a different reference patch which had its phase already determined. This caused discontinuities in the measured phase. A second alternative was to divide the pixels on a 1:1 ratio between the two patches in the overlapping region (I chose a checkerboard pattern) which produced consistent results. After gathering phase data into a two-dimensional phase map the phase map was

unwrapped using an algorithm mapping the phase unwrapping problem to a network flow problem ([1]).

A small remark on fitting: When fitting this term to the voltages received, I had to make sure that the cosine amplitude has a non-negative lower limit. Otherwise values of φ_0 around π will cause the amplitude to go to negative values (simple linear dependencies are found most quickly by the underlying optimizer) and φ_0 will have an offset of π .

6 Image Analysis of Example Patterns

For performance evaluation various amplitude distributions were transformed into phase patterns using the IFTA algorithm (4.2) and then applied to the SLM in the setup (??). The destination plane amplitude patterns were then imaged using a beam profile camera. These images were then analyzed to evaluate performance characteristics of the computation and imaging tool-chain.

6.1 Point Spread Function

The point spread function of the setup can be measured by simply putting a diffraction grating (to steer the beam toward the output arm). Ideally, this projects a collimated beam onto the objective lens. The objective lens then focuses this beam into a single point. Due to the limited aperture, optical aberrations in imaging and small deformations of the modulator, the focus is distorted. However, the phase distortions induced should be captured by the measurement in section 5.3.3. Adding an opposite phase to the grating pattern compensates for this distortion and readjusts the focus. To demonstrate this effect two pictures of the focal plane intensity distribution were taken with a Coherent LaserCam HR beam profile camera. The first picture in figure 29 shows the distribution when no phase correction is applied. After adding a phase correction onto the diffraction grating (which is simply the additive inverse of the phase map measured during calibration) the intensity distribution changes into a more strongly focused one.

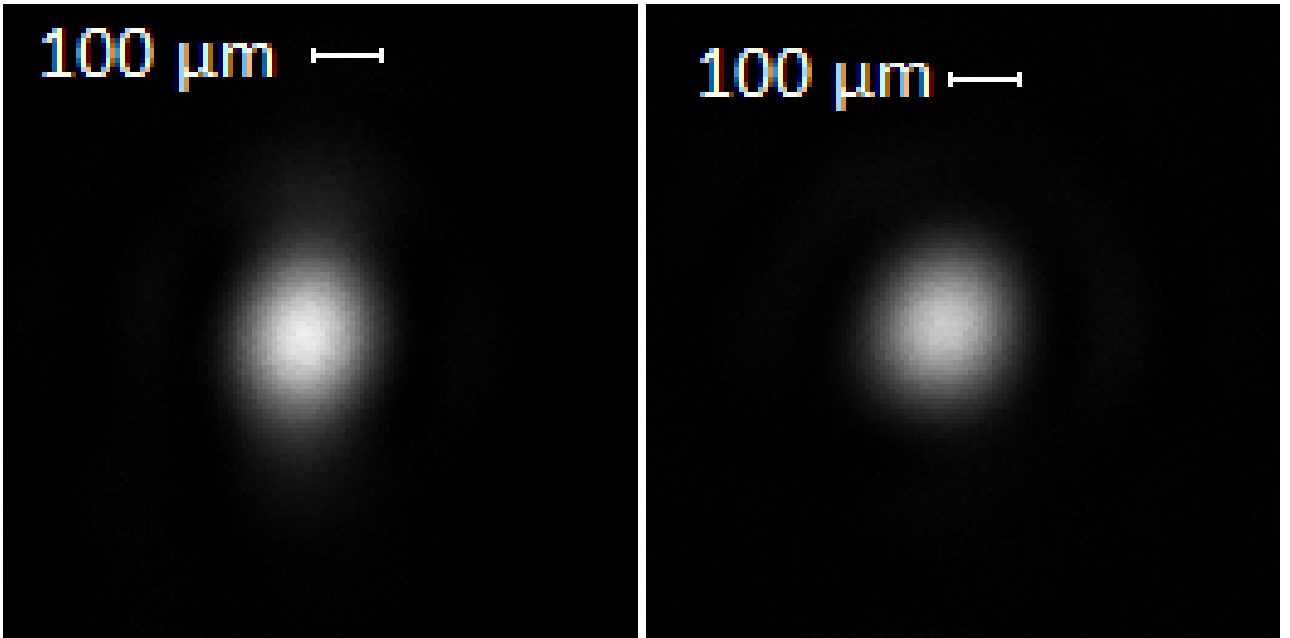


Figure 29: Single point images for uncorrected (left) and corrected (right) images

Analyzing the picture visually gives a conservative estimate of the radius of $100 \mu\text{m} \pm 20 \mu\text{m}$. The objective aperture is defined by a blend placed directly behind it. This blend

was set to an aperture diameter $d_{\text{Aperture}} = 1.15 \pm 0.1$ cm. The diffraction limit for the point radius is given by $r_{\text{Abbe}} = \frac{d}{2} = \frac{\lambda}{2n \sin(\theta)}$ with $\sin(\theta) = \frac{d_{\text{Aperture}}}{2f}$, $n = 1$, $\lambda = 852$ nm and $f = 1$ m. The Abbe radius then evaluates as $r_{\text{Abbe}} = 74 \pm 7$ μm . Comparing this to the measured radius shows that the setup might be operating in diffraction limit.

6.2 Four Points

To evaluate the performance on optical tweezer applications, four points were placed in a cross pattern around the image center. These points were spaced 10 pixels from the center in the target image, which corresponds to an expected distance of $r_{xy} = 10f \frac{f_1}{f_2} \frac{\lambda}{d_{\text{Modulator},xy}}$ from the center (since the individual Fourier modes are addressed by $\sin(\theta) \cdot d_{\text{Modulator}} = n \cdot \lambda$). Here $\frac{f_2}{f_1} = 2$ is the magnification ratio of the modulator imaging telescope. These values evaluate to:

$$\begin{aligned} r_x &= 10 \cdot 1 \text{ m} \cdot \frac{1}{2} \cdot \frac{852 \text{ nm}}{14.98 \text{ mm}} \\ &= 569 \text{ } \mu\text{m} \\ r_y &= 10 \cdot 1 \text{ m} \cdot \frac{1}{2} \cdot \frac{852 \text{ nm}}{10.92 \text{ mm}} \\ &= 780 \text{ } \mu\text{m} \\ \frac{r_y}{r_x} &= 1.367 \end{aligned}$$

An experimental measurement of this output distribution can be seen in figure 30. The centers were estimated graphically. To estimate measurement errors, the size of the brightest center regions was estimated at 7x7 pixels which results in a 7 pixel error estimate for spot positions. By subtracting spot positions, the following estimates were obtained:

$$\begin{aligned} 2 \cdot r_x &= 940 \pm 47 \text{ } \mu\text{m} \\ 2 \cdot r_y &= 1264 \pm 47 \text{ } \mu\text{m} \\ \frac{r_y}{r_x} &= 1.34 \pm 0.08 \end{aligned}$$

While the image proportions are as expected, the size does not match. The magnification ratio seems to differ by a factor of $\frac{\text{Meas}[r_x] + \text{Meas}[r_y]}{r_x + r_y} = 0.82 \pm 0.03$ from the expected magnification of 2. This can be attributed to the telescope not operating in 2f+2f-configuration.

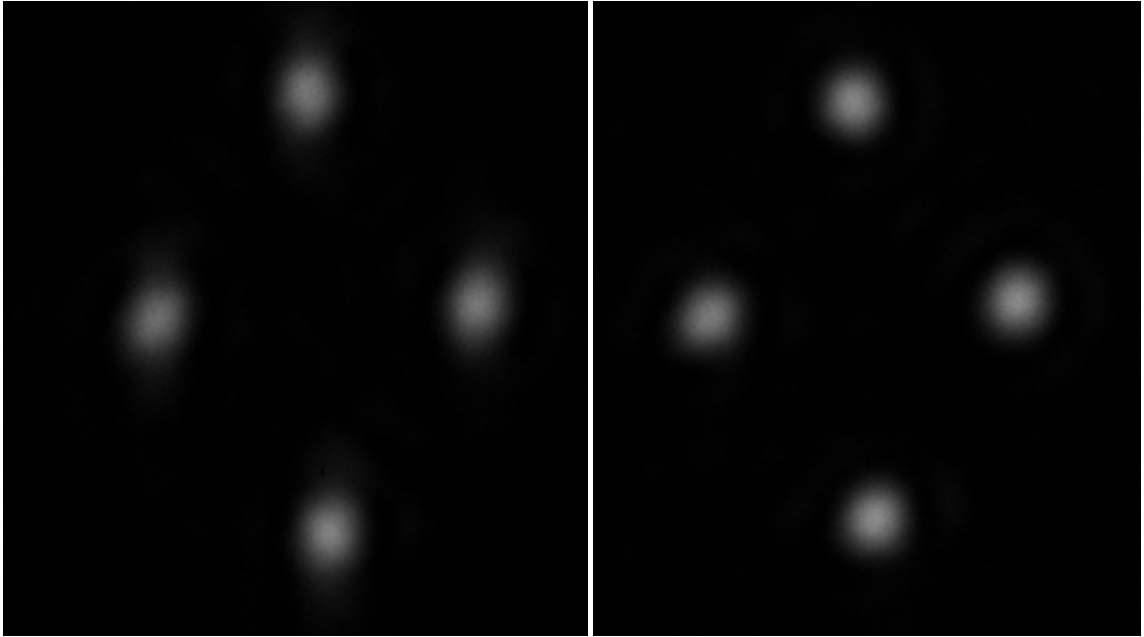


Figure 30: Four dot cross pattern without (left) and with (right) phase correction

6.3 Rectangular pattern

The next pattern to be generated was chosen as a filled square, which ideally should result in a filled rectangle visible on the camera. However, as can be seen in figure 31, the interior filling of the square does not work. This problem is not apparent IFTA image computation, as the expected amplitude distribution (computed as the Fourier transform of the beam profile with the intended phase modulation) is to a high degree homogeneous. Potential causes for this are distortions by the imaging system or effects on a narrower scale than the angular distance of the grid produced by the discrete Fourier transform. Additionally, the discrete Fourier transform assumes periodicity of input and output data which is not given. Also there could be phase vortex caused distortions on a scale not resolved by the discrete Fourier transform which get modified and therefore visible on larger scales by the imaging optics.

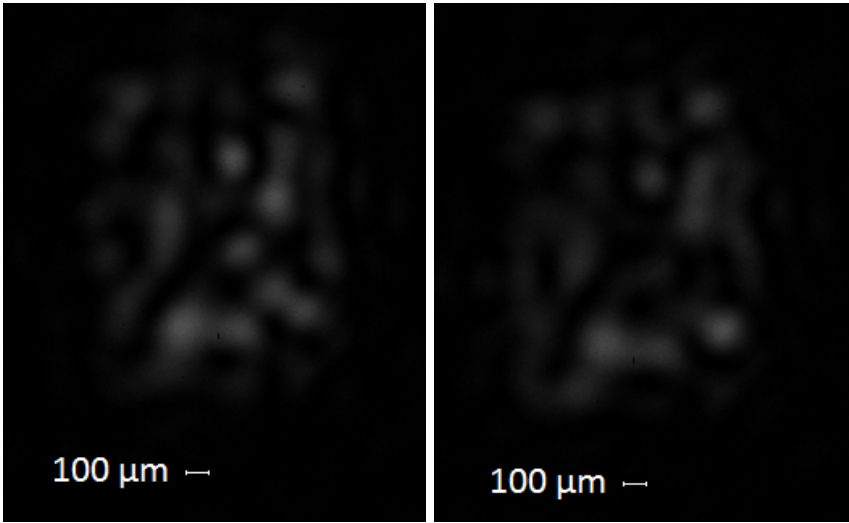


Figure 31: Distorted rectangular pattern without (left) and with (right) phase correction

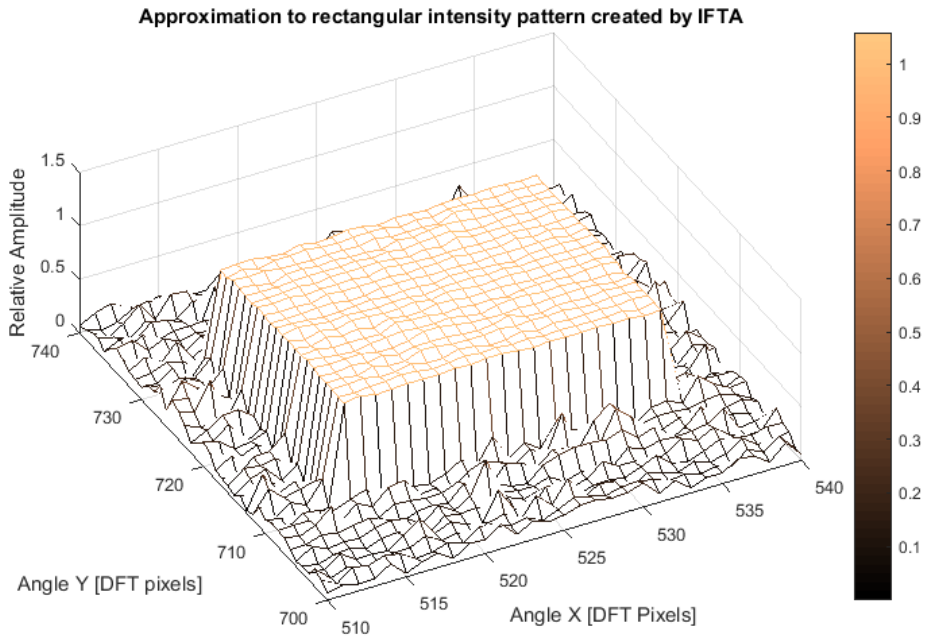


Figure 32: Computed far field shape for the rectangular pattern

6.4 Complex Binary Shape

In order to verify the ability to handle complex structures, a known symbol well suited for projection was taken as a reference image (see fig. 33). The image bitmap was then used as a target shape to recreate a phase pattern from. The physical implementation of the pattern can be seen in figure 34. As evident, the same problem as in section 6.3 persists here as well. However, the dark sections of the image seem to be well reproduced up to and including the edges.

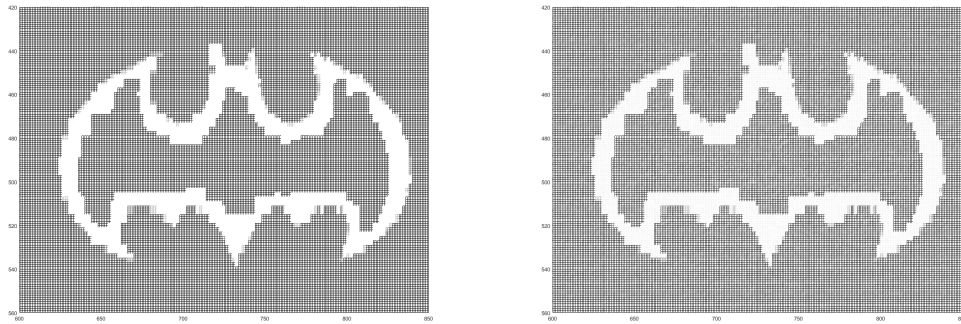


Figure 33: Desired (left) vs expected (as in predicted by the computation) output (right) amplitude distribution for Batman logo

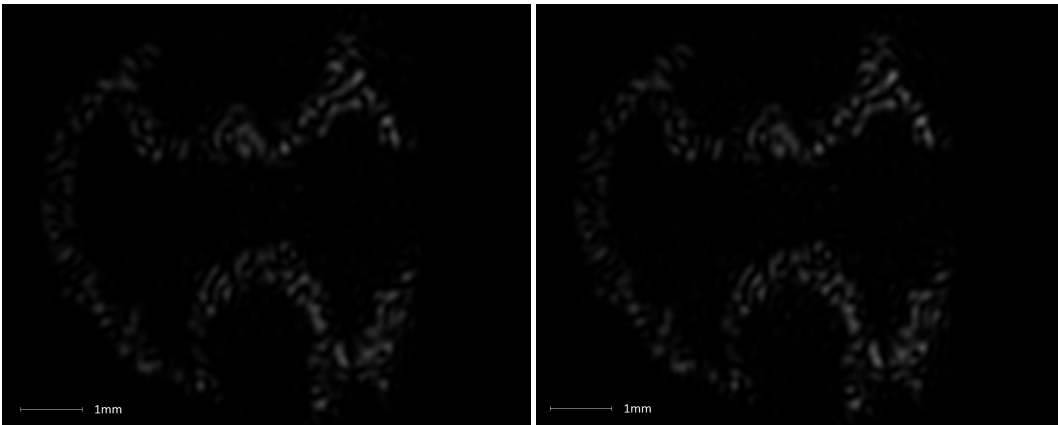


Figure 34: Measured amplitude distribution without (left) and with (right) phase distortion compensation

To determine possible causes of these surface inhomogeneities, I placed the beam profile camera right in front of the objective. Since the telescope is configured geometrically to image the modulator onto the objective and the modulator modulates only the light's phase one would expect to see a magnified beam profile on the objective. If the modulator only displays a constant phase shift everywhere (and is tilted to direct the beam into the imaging section of the telescope), this is the case. However, the pattern one gets when putting an

image phase pattern onto the modulator looks distinctly different as can be seen in figure 35. When removing the image phase modulation but retaining the diffraction grating pushing the beam away from the 0th-order reflection, one obtains a different pattern that can be seen in figure 36.

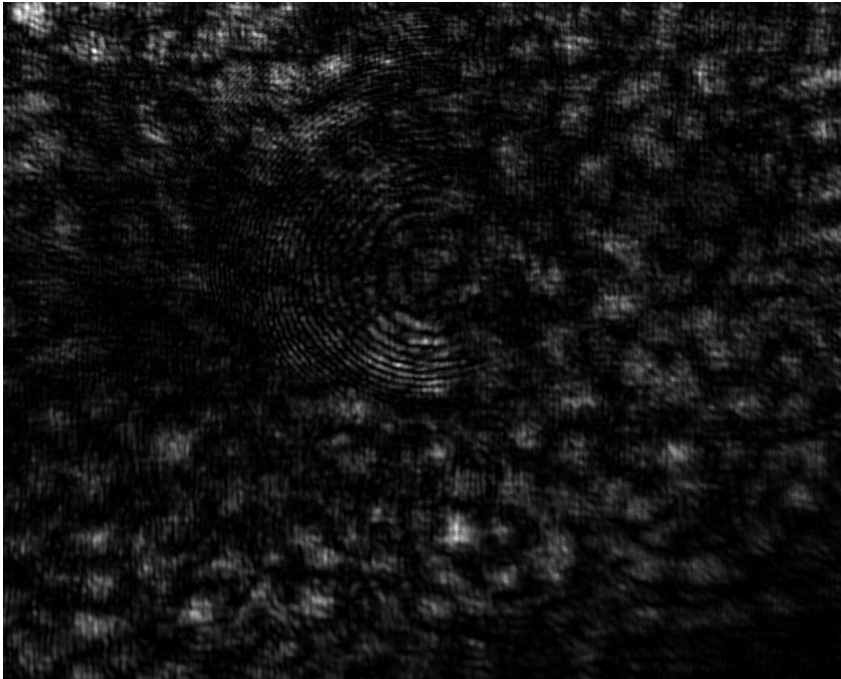


Figure 35: Intensity distribution on objective for Batman-Logo phase pattern



Figure 36: Intensity distribution on objective for diffraction grating (and phase correction)

6.5 Square in Alternative Imaging Configuration

In order to determine whether the distortions in the image were caused primarily by the imaging system, the system was reconfigured for imaging in $2f + 2f$ configuration (see section 5.1.1), calibrated, and the problematic measurements repeated. The results of this measurement can be seen in figure 37. Even when factoring out the higher contrast of this image compared to figure 31 – the camera had to be readjusted after changing the lens configuration – the images taken here seem to have a finer-grained feature resolution.

6.6 Complex Binary Shape in Alternative Imaging Configuration

I also repeated the measurement of the batman logo in $2f + 2f$ configuration (see section 5.1.1). As shown in figure 38 the resolution of the imaging distortions has improved compared to figure 34. When examining the corner sections in comparison of the left and right part figure there also seems to show an improvement in contrast and edge sharpness when phase distortion compensation is applied. These effects can possibly be attributed to the reduced imaging aberrations for central modulator pixels (see section 5.2) compared to the far objective configuration. This would be especially plausible if the source of the dark areas are narrow phase discontinuities which are widened by imaging aberrations. Additionally, when comparing the images with and without phase compensation, one can see small light spots appearing in previously dark areas when phase distortion compensation is used. This side effect of the compensation required further investigations, as all previous trials had shown an improved edge sharpness when applying phase correction.

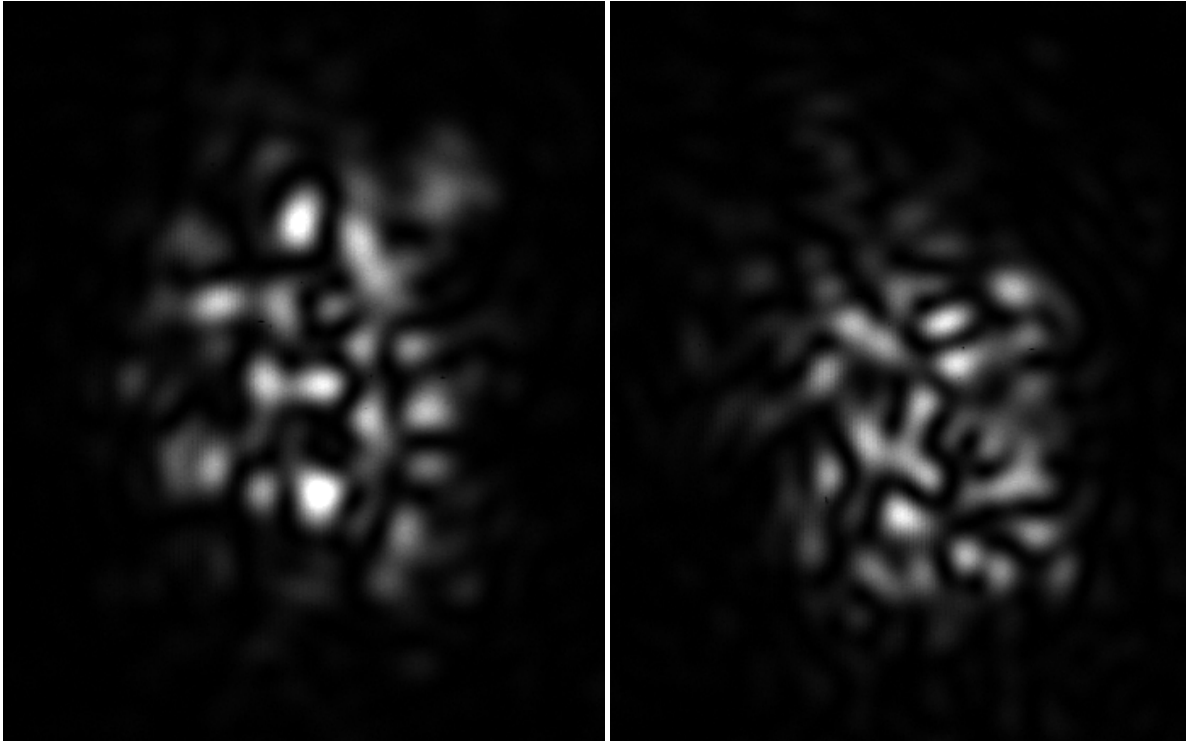


Figure 37: Measurement of the distorted rectangle image for the $2f+2f$ imaging system with (right) and without (left) phase compensation

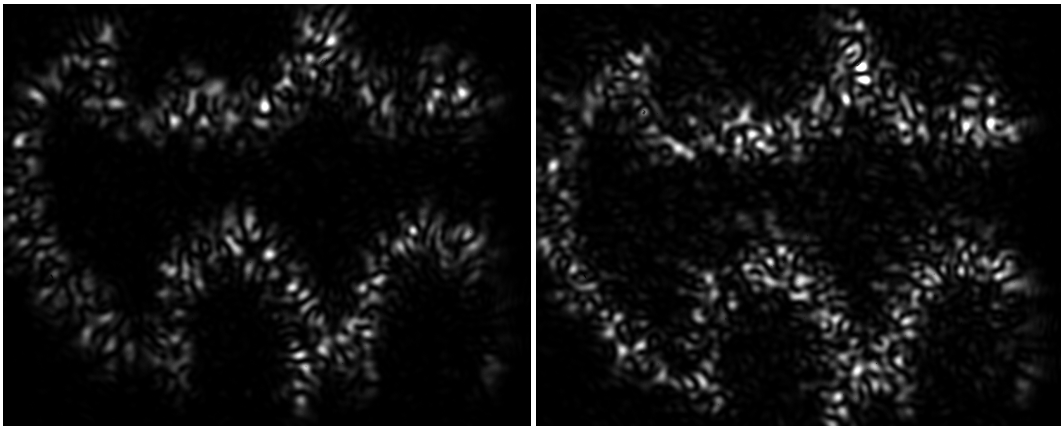


Figure 38: Measurement of the batman logo in $2f+2f$ imaging configuration without (left) and with (right) phase distortion compensation

7 Summary and Outlook

In this thesis I evaluated different Liquid Crystal on Silicon Spatial Light Modulators for their phase noise characteristics and implemented a first iteration of an inline holography scheme for the Santec SLM 100. When evaluating the performance of this implementation, point and edge sharpness were found to be of sufficient quality (in the diffraction limit of the optical imaging system) while homogeneity of illuminated areas left a lot to be desired. For an outlook I would like to present multiple future options to improve the system on this front:

- The imaging system still has significant off-axis aberrations. The primary suggestion for improvement here would be to switch from the currently used plane-convex singlet lenses to aberration-corrected multi-element lenses. These are available commercially at a large variety of wavelength coatings and focal lengths.
- While stability of the image seems to be good in the discrete Fourier transform part of the Iterative Fourier Transform algorithm, there might still be significant problems caused by phase vortices on shorter angular scales not resolved by the discrete Fourier transform. One suggestion would be to enhance the iteration by a phase vortex removal scheme as presented in [28]. Alternatively or additionally one can introduce regularization into the iteration to prevent the algorithm from early convergence into short-term effective solutions which turn out suboptimal on later iterations (see [16])
- An additional option would also be to migrate to a more advanced imaging scheme where the modulator is used in a double pass configuration. First, one side of the modulator is illuminated by the input beam. The first diffraction order is directed onto a spherical mirror, which performs a Fourier transform and directs the Fourier transformed wavefront back onto the modulator. Here it is modulated again and the result is then directed towards the imaging objective (which performs another Fourier transform). This double-pass configuration allows the modification of the wavefront amplitude as well as phase before phase modulation and therefore significantly eases the condition of the IFTA problem. Out of all reviewed schemes it is the most complex but also the most promising implementation. A closer look can be found in the original presentation in [14].

References

- [1] A phase unwrapping method based on network programming. In *ERS SAR interferometry, Proceedings of the Fringe 96 Workshop, held in Zurich, Switzerland, 30 September-2 October 1996. Edited by T.-D. Guyenne and D. Danesy. ESA SP-406. Paris: European Space Agency*, page 261, 1997.
- [2] *Raman Scattering and Other Multiphoton Processes*, pages 417–445. Springer Berlin Heidelberg, Berlin, Heidelberg, 2007.
- [3] C.S. Adams and E. Riis. Laser cooling and trapping of neutral atoms. *Progress in Quantum Electronics*, 21(1):1 – 79, 1997.
- [4] Mikael P. Backlund, Matthew D. Lew, Adam S. Backer, Steffen J. Sahl, Ginni Grover, Anurag Agrawal, Rafael Piestun, and W. E. Moernerb. The double-helix point spread function enables precise and accurate measurement of 3d single-molecule localization and orientation. *Proceedings of SPIE The International Society for Optical Engineering*, 2013.
- [5] Dirk Bouwmeester, Artur K. Ekert, and Anton Zeilinger. *The Physics of Quantum Information*. Springer, 2000.
- [6] Stefan Brakhane. *The Quantum Walk Microscope*. PhD thesis, Rheinische Friedrich Wilhelm Universität Bonn, 2016.
- [7] Jun Chen, Tsukasa Hirayama, Kazuo Ishizuka, and Akira Tonomura. Spherical aberration correction using a liquid-crystal spatial-light modulator in off-axis electron holography. *Appl. Opt.*, 33(28):6597–6602, Oct 1994.
- [8] Jennifer E. Curtis, Brian A. Koss, and David G. Grier. Dynamic holographic optical tweezers. *Optics Communications*, 207(1-6):169 – 175, 2002.
- [9] Ken A. Dill and Justin L. MacCallum. The protein-folding problem, 50 years on. *Science*, 338(6110):1042–1046, 2012.
- [10] Jiangfeng Du, Nanyang Xu, Xinhua Peng, Pengfei Wang, Sanfeng Wu, and Dawei Lu. Nmr implementation of a molecular hydrogen quantum simulation with adiabatic state preparation. *Phys. Rev. Lett.*, 104:030502, Jan 2010.
- [11] Richard P. Feynman. Simulating physics with computers. *International Journal of Theoretical Physics*, 21(6):467–488, 1982.
- [12] R. W. Gerchberg and W. O. Saxton. A practical algorithm for the determination of phase from image and diffraction plane pictures. *Optik*, 35(2):237–246, 1972.
- [13] Larry J. Hornbeck. Current status and future applications for dmd-based projection displays. *Proceeding of Fifth International Display Workshop*, pages 1–4, 1998.
- [14] Alexander Jesacher, Christian Maurer, Andreas Schwaighofer, Stefan Bernet, and Monika Ritsch-Marte. Near-perfect hologram reconstruction with a spatial light modulator. *Opt. Express*, 16(4):2597–2603, Feb 2008.

- [15] Michal Karski, Leonid Förster, Jai-Min Choi, Andreas Steffen, Wolfgang Alt, Dieter Meschede, and Artur Widera. Quantum walk in position space with single optically trapped atoms. *Science*, 325(5937):174–177, 2009.
- [16] Hwi Kim, Byungchoon Yang, and ByoungHo Lee. Iterative fourier transform algorithm with regularization for the optimal design of diffractive optical elements. *J. Opt. Soc. Am. A*, 21(12):2353–2365, Dec 2004.
- [17] K. Kim, M.-S. Chang, S. Korenblit, R. Islam, E. E. Edwards, J. K. Freericks, G.-D. Lin, L.-M. Duan, and C. Monroe. Quantum simulation of frustrated ising spins with trapped ions. *Nature*, 2010.
- [18] Ryuji Kimura. Numerical weather prediction. *Journal of Wind Engineering and Industrial Aerodynamics*, 90(12):1403–1414, 2002.
- [19] Adam Lopez. Statistical machine translation. *ACM Comput. Surv.*, 40(3):8:1–8:49, August 2008.
- [20] D. Lu and Q. Weng. A survey of image classification methods and techniques for improving classification performance. *International Journal of Remote Sensing*, 28(5):823–870, 2007.
- [21] Henry Markram. The blue brain project. *Nature Reviews. Neuroscience*, 2006.
- [22] Hagai B. Perets, Yoav Lahini, Francesca Pozzi, Marc Sorel, Roberto Morandotti, and Yaron Silberberg. Realization of quantum walks with negligible decoherence in waveguide lattices. *Phys. Rev. Lett.*, 100:170506, May 2008.
- [23] Carsten Robens. *Testing the Quantumness of Atomic Trajectories*. PhD thesis, Rheinische Friedrich Wilhelm Universität Bonn, 2016.
- [24] Carsten Robens, Wolfgang Alt, Dieter Meschede, Clive Emary, and Andrea Alberti. Ideal negative measurements in quantum walks disprove theories based on classical trajectories. *Phys. Rev. X*, 5:011003, Jan 2015.
- [25] Carsten Robens, Stefan Brakhane, Wolfgang Alt, Felix Kleißler, Dieter Meschede, Geol Moon, Gautam Ramola, and Andrea Alberti. High numerical aperture (na=?0.92) objective lens for imaging and addressing of cold atoms. *Opt. Lett.*, 42(6):1043–1046, Mar 2017.
- [26] Carsten Robens, Stefan Brakhane, Dieter Meschede, and A. Alberti. *Quantum Walks with Neutral Atoms: Quantum Interference Effects of One and Two Particles*, pages 1–15. WORLD SCIENTIFIC, 2016.
- [27] A. Savitzky and M.J.E. Golay. Smoothing and differentiation of data by simplified least squares procedures. *Analytical Chemistry*, 36:1627–1639, 1964.
- [28] Paramasivam Senthilkumarana, Frank Wyrowskib, and Hagen Schimmelb. Vortex stagnation problem in iterative fourier transform algorithms, 2004.
- [29] Daniel A. Steck. Cesium d line data. Available online at <http://steck.us/alkalidata>, December 2010.

- [30] J. Struck, C. Ölschläger, R. Le Targat, P. Soltan-Panahi, A. Eckardt, M. Lewenstein, P. Windpassinger, and K. Sengstock. Quantum simulation of frustrated classical magnetism in triangular optical lattices. *Science*, 333(6045):996–999, 2011.
- [31] Gregor Thalhammer, Richard W. Bowman, Gordon D. Love, Miles J. Padgett, and Monika Ritsch-Marte. Speeding up liquid crystal slms using overdrive with phase change reduction. *Opt. Express*, 21(2):1779–1797, Jan 2013.
- [32] Salvador Elías Venegas-Andraca. Quantum walks: a comprehensive review. *Quantum Information Processing*, 11(5):1015–1106, 2012.
- [33] F. Zähringer, G. Kirchmair, R. Gerritsma, E. Solano, R. Blatt, and C. F. Roos. Realization of a quantum walk with one and two trapped ions. *Phys. Rev. Lett.*, 104:100503, Mar 2010.
- [34] Zheng You1 Zichen Zhang and Daping Chu. Fundamentals of phase-only liquid crystal on silicon (lcos) devices. *Light: Science & Applications*, 3, 2014.
- [35] Philip P. J. Zupancic. Dynamic holography and beamshaping using digital micromirror devices. Master’s thesis, Ludwig-Maximilians-Universität München, 2013.

Acknowledgements

Given that a master thesis corresponds to a year-long project, I would really like to thank my family – especially my aunt – for always keeping my back open so that I could find the necessary time.

During the last year I had the opportunity to get a glimpse into the practical implementation of science. I would like to thank Prof. Dr. Dieter Meschede for giving me this opportunity to work in his research group. I also thank Dr. Elisabeth Soergel for her willingness to take over the second advisorship of this thesis on short notice. Andrea Alberti provided me with this interesting project and was always available with his expertise, especially concerning theoretical matters and their link to the experiment. Wolfgang Alt was always willing to share his large experience with electronics and optics. Andrea and Wolfgang provided joint supervision to me and I want to thank them for always taking their time out of important matters for this.

A special mention goes to Carsten Robens. Not only did he provide me with a lot of best practices in project planning and experimental techniques, but his mind also contains a complete copy of the *Chicago Manual of Style*. His feedback on this thesis was invaluable in getting it to its current point.

Building an extension to an existing experiment only works when you are in contact with those who know it inside-out. For always being available for questions, even during alignment procedures, I would like to thank Stefan Brakhane, Goel Moon and Gautam Ramola. An additional recognition here goes towards Richard Winkelmann, who will be taking over this project and who also had a hand in various technical aspects of it. Also, he and the other people working in the same office with me, especially Manolo Rivera Lam and Natalie Thau, always provided me with useful remarks and engaging conversations on various topics in- and outside of physics.

Additional thanks go to Dietmar Haubruch, Fien Latumahina and Annelise von Rudloff-Miglo for backing me up in all matters administrative and to our fine mechanics workshop for providing the required custom parts at high quality.

Declaration of Authorship

I hereby declare that the work presented here was formulated by myself and that no sources or tools other than those cited were used.

Bonn, den _____
date

Unterschrift: _____
signature